

AD-A112 377

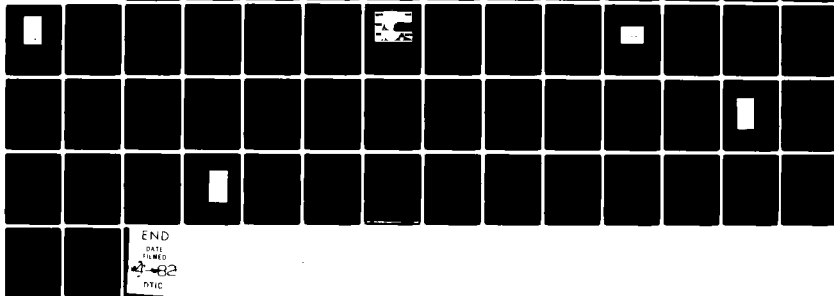
CALIFORNIA UNIV LOS ANGELES DEPT OF ELECTRICAL ENG--ETC F/8 20/9
WAVES AND INSTABILITIES IN STEADY-STATE HIGH BETA PLASMAS. (U)
DEC 81 N C LUHMANN F49620-76-C-0012
UCLA-ENG-81-48

UNCLASSIFIED

AFOSR-TR-82-0178

NL

For
Access



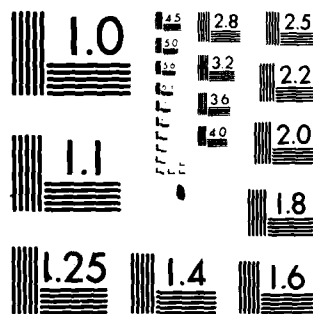
END

DATE

FILMED

4-82

DTIC



MICROCOPY RESOLUTION TEST CHART
NATIONAL BUREAU OF STANDARDS 1963-A

(12)

AD A112377

FINAL REPORT

Research conducted by the
The Space Office of the University of California
at Los Angeles, California, USA
under contract to AFOSR

F47620 96-0-0012

DTIC
MAR 23 1982
H

WAVES AND INSTABILITIES IN STEADY STATE
HIGH BETA PLASMAS

UCLA-ENG-81-48
DECEMBER 1981

Principal Investigator: N.C. Luhmann, Jr.
Professor

FILE COPY

Approved for public release;
distribution unlimited.

22 22 22 122

12

UCLA-ENG-81-48
DECEMBER 1981

FINAL SCIENTIFIC REPORT

WAVES AND INSTABILITIES IN STEADY STATE HIGH BETA PLASMAS

PRINCIPAL INVESTIGATOR: N.C. Luhmann, Jr.
Professor

Research sponsored by the
Air Force Office of Scientific Research
Air Force Systems Command, USAF,
under Contract No. ~~F49620-76-C-0012~~

F49620-76-C-0012

DTIC
MAR 23 1982
D

Electrical Engineering Department
School of Engineering and Applied Science
University of California
Los Angeles, California 90024

AIR FORCE OFFICE OF SCIENTIFIC RESEARCH (AFSC)
NOTICE OF CONFIDENTIALITY TO DTIC
This technical report has been reviewed and is
approved for public release in accordance with AFM 11-12.
Distribution is unlimited.
MATTHEW S. KEMNER
Chief, Technical Information Division

REPORT DOCUMENTATION PAGE		READ INSTRUCTIONS BEFORE COMPLETING FORM
1. REPORT NUMBER AFOSR-TR- 82 -0178	2. GOVT ACCESSION NO. AD-A112 377	3. RECIPIENT'S CATALOG NUMBER
4. TITLE (and Subtitle) Waves and Instabilities in Steady-State High Beta Plasmas		5. TYPE OF REPORT & PERIOD COVERED FINAL SCIENTIFIC REPORT
7. AUTHOR(s) N. C. Luhmann, Jr.		6. PERFORMING ORG. REPORT NUMBER UCLA-ENG-81-48
8. PERFORMING ORGANIZATION NAME AND ADDRESS Electrical Engineering Department 7702 Boelter Hall, UCLA, Los Angeles, CA 90024		8. CONTRACT OR GRANT NUMBER(s) US AFOSR Contract F49620-76-C-0012
11. CONTROLLING OFFICE NAME AND ADDRESS AFOSR 410 Edwards AFB, CA 93522		10. PROGRAM ELEMENT, PROJECT, TASK AREA & WORK UNIT NUMBERS 611021- 2301/48
14. MONITORING AGENCY NAME & ADDRESS (if different from Controlling Office)		12. REPORT DATE December 1981
		13. NUMBER OF PAGES 52
		15. SECURITY CLASS. (of this report) Unclassified
		15a. DECLASSIFICATION DOWNGRADING SCHEDULE
16. DISTRIBUTION STATEMENT (of this Report) Approved for public release; distribution unlimited		
17. DISTRIBUTION STATEMENT (of the abstract entered in Block 20, if different from Report)		
18. SUPPLEMENTARY NOTES		
19. KEY WORDS (Continue on reverse side if necessary and identify by block number) Microwave Experimental Simulation of Laser-Plasma Interactions Stimulated Brillouin Scattering Optical Mixing Resonance Absorption Hot Electron Production (Cont. on next page)		
20. ABSTRACT (Continue on reverse side if necessary and identify by block number) Experimental simulations of laser-plasma interactions have been performed in the microwave region. Stimulated Brillouin scattering from transient density perturbations associated with the finite (1%) chamber reflectivity has been observed. Saturation of the reflectivity has been observed at ~ 5% and the saturation mechanism identified as ion tail heating. The experimental results are in excellent agreement with numerical calculations of the density fluctuations and reflectivity which account for electron main body heating via inverse Bremsstrahlung absorption and ion tail heating. (Cont. on next page)		

DD FORM 1 JAN 73 1473

19. Key Words (Cont.)

Finite Bandwidth Control
Cold Plasma Wavebreaking

20. Abstract (Cont.)

For the first time ion waves have been generated by optical mixing. The experimental results in the linear region were shown to be in excellent agreement with theoretical predictions. The saturation level was found to be identical to that seen in the "pure" SBS studies and shown to be also due to ion tail heating.

Studies were made of resonance absorption produced electric fields and the associated hot electron production. At the lowest intensity levels the saturation was shown to be due to plasma wave convection out of the critical layer while at higher intensities it was due to cold plasma wavebreaking. Finally, finite bandwidth effects were investigated.



Accession For	
NTIS OF AI	<input checked="checked" type="checkbox"/>
FORM T-8	<input type="checkbox"/>
1.000000	<input type="checkbox"/>
0.000000	
2.000000	
3.000000	
4.000000	
5.000000	
6.000000	
7.000000	
8.000000	
9.000000	
10.000000	
11.000000	
12.000000	
13.000000	
14.000000	
15.000000	
16.000000	
17.000000	
18.000000	
19.000000	
20.000000	
21.000000	
22.000000	
23.000000	
24.000000	
25.000000	
26.000000	
27.000000	
28.000000	
29.000000	
30.000000	
31.000000	
32.000000	
33.000000	
34.000000	
35.000000	
36.000000	
37.000000	
38.000000	
39.000000	
40.000000	
41.000000	
42.000000	
43.000000	
44.000000	
45.000000	
46.000000	
47.000000	
48.000000	
49.000000	
50.000000	
51.000000	
52.000000	
53.000000	
54.000000	
55.000000	
56.000000	
57.000000	
58.000000	
59.000000	
60.000000	
61.000000	
62.000000	
63.000000	
64.000000	
65.000000	
66.000000	
67.000000	
68.000000	
69.000000	
70.000000	
71.000000	
72.000000	
73.000000	
74.000000	
75.000000	
76.000000	
77.000000	
78.000000	
79.000000	
80.000000	
81.000000	
82.000000	
83.000000	
84.000000	
85.000000	
86.000000	
87.000000	
88.000000	
89.000000	
90.000000	
91.000000	
92.000000	
93.000000	
94.000000	
95.000000	
96.000000	
97.000000	
98.000000	
99.000000	
100.000000	

I. INTRODUCTION

The aim of the UCLA microwave modeling program is to employ high power (0.1 - 10 MW) microwave sources ($\lambda_0 = 10$ cm) and well-diagnosed low density ($n_e = 10^{10}$ - 10^{12} cm $^{-3}$) plasma devices to perform experimental simulations of important aspects of laser-pellet and laser-plasma focus interactions. The purpose of these simulations is three-fold. First, microwave modeling permits one to isolate important physics issues. An example is our recent confirmation of the role of ion tail heating in SBS saturation. The second is to inexpensively test new ideas (i.e. finite bandwidth control). The third purpose is to develop a vehicle in which testing and normalization of computer codes can be done. This obviously permits one to gain more confidence in scaling code results to other wavelengths, intensities, etc.

In order to perform such simulations as mentioned above, one requires that certain key parameter scalings be maintained. Exactly which ones are essential is, of course, a function of the process under investigation. In general, however, the important parameters are $v_0/v_{te} = eE_0/m_0v_{te}$, v_0/c , $E_0^2/8\pi n_e K T_e$, $\omega_s \tau_p$ and L/λ_0 . Here E_0 is the vacuum field strength of the pump (frequency ω_0 , wavelength λ_0), L is the density gradient scalelength, ω_s an appropriate acoustic frequency, τ_p is the pulse duration and v_{te} is the electron thermal velocity. One of the most difficult scalings to maintain is that for $\omega_s \tau_p$. Basically, here we must run the experiment for a sufficiently large number of hydrodynamic timescales to observe such phenomena as profile steepening and plateau formation or stimulated Brillouin scattering growth from noise. Since these low density laboratory plasma tend to be weakly-

ionized ($\approx 1-10\%$) there is a maximum employable rf pulse duration (power and plasma density dependent) beyond which appreciable ionization of the neutral gas background and target plasma modification occurs.

During the past year we have devoted considerable effort toward experimental arrangements which best satisfy the above-mentioned scaling criteria. Here we have been forced to adopt measures similar to the computer simulationist who, for example, begins with a steepened profile in order to save computer time. Fortunately, there appear to be several approaches which permit us to study the saturation (as well as the growth) of SBS, SRS, as well as resonance absorption. For example, in the case of the SBS studies two approaches were used. The first depended upon our amplifying an enhanced noise level (transient ion wave produced by chamber reflections). Since we were not growing from thermal fluctuations we required a shorter duration rf pulse to reach a given fluctuation level. The second approach involved the use of optical mixing. Here we drove both SBS electromagnetic waves with a frequency separation equal to the ion acoustic frequency. This reduced the rf drive requirements (to observe saturation) by one to two orders of magnitude allowing values of $\omega_p \tau_p$ as large as 6×10^3 which roughly corresponds to a 1 nsec duration Nd glass laser pulse. Saturation levels similar to those observed with the first approach were obtained.

Throughout the current contract period we have concentrated on two distinct problem areas: Stimulated Brillouin Scattering (SBS) and resonance absorption produced hot electrons. Very briefly, our results to date are as follows:

1. Observation of the saturation of SBS growth from chamber reflectivity induced background density fluctuations.^(1,2)
2. Conclusive identification of the dominant SBS saturation mechanism as ion tail heating.

3. First observation of optical mixing produced ion acoustic waves.
4. Observation of saturation of optical mixing produced ion acoustic waves at the same level as in SBS studies -- identification of ion heating as the sole saturation mechanism.
5. Observation of cold plasma wavebreaking saturation of resonance absorption produced electric fields.
6. Finite bandwidth control of resonance absorption electric fields and hot electron production.

II. RESULTS DURING CURRENT CONTRACT PERIOD

As mentioned in Sec. I, throughout the current contract period we have concentrated on two distinct problem areas: Stimulated Brillouin Scattering (SBS) and resonance absorption produced hot electrons. The SBS studies were further subdivided into the "pure" SBS growth case and the optical mixing case where both of the electromagnetic waves ("incident" and "reflected") were driven. The latter case allowed us to observe saturation of the ion waves at significantly lower incident rf power levels than in the "pure" SBS case. This permitted us to greatly increase the pulse duration ($\omega_p \tau \leq 10^4$) and to insure that our experimental simulations were relevant on the laser fusion timescale.

A. STIMULATED BRILLOUIN SCATTERING

During the past few years we have investigated the growth and saturation of SBS in an underdense plasma ($n = 0.1 n_c$). Before concentrating on our more recent results, it will prove helpful to briefly describe the experimental arrangement as well as the major past accomplishments.

The experimental arrangement for the SBS studies is shown schematically in Fig. 1. Microwave radiation ($\lambda_0 = 1 - 11$ cm) is launched along the axis of a relatively uniform ($L_D = 4m$, $L_T = 20m$) underdense plasma. In the studies to date, the density has been held constant at $0.1 n_c$ to avoid the possibility of other competing instabilities confusing the interpretation of the experimental

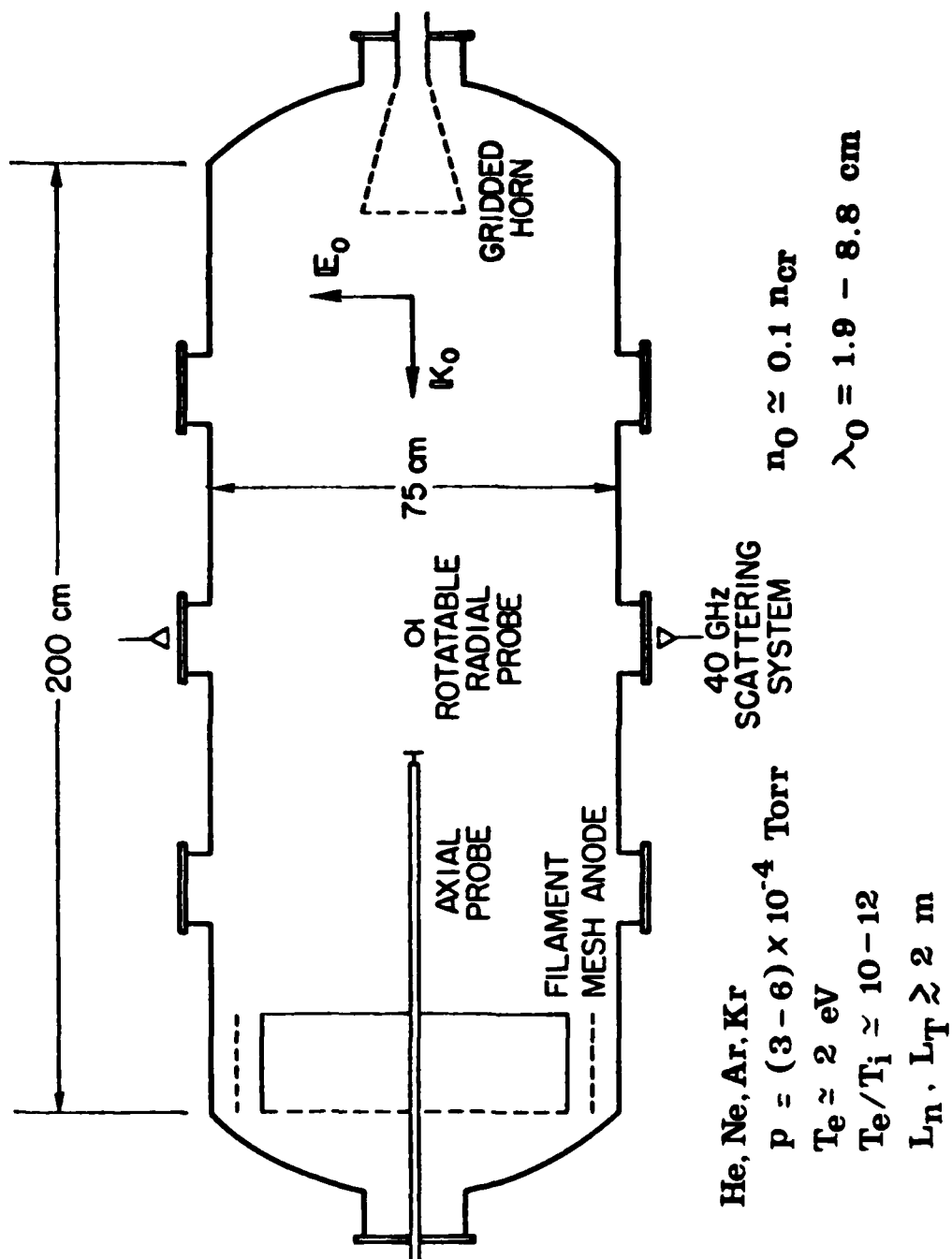


Fig. 1 Experimental Arrangement for Brillouin Backscatter Studies.

results.

Although microwave absorber was placed on the chamber endwalls to reduce reflections, it was found that the residual 1% reflectivity had a large influence on the system behavior. Specifically, it was found that "switching on" the partial standing electromagnetic wave pattern led to a transient ion acoustic perturbation of the form:⁽¹⁻⁴⁾

$$\bar{n}(x,t)/n_0 = r^{1/2} (v_0/v_{te})^2 [1 - \frac{\nu}{\omega_s} e^{-\nu t} \sin \omega_s t - e^{-\nu t} \cos \omega_s t] \cos 2k_0 x$$

For short times this is given approximately by

$$\bar{n}(x,t)/n_0 = r^{1/2} (v_0/v_{te})^2 (1 - \cos \omega_s t) \cos 2k_0 x$$

This can obviously be decomposed into a zero frequency density perturbation together with a right and left propagating ion wave. The incident wave Thomson scattering from the ion perturbation resulting in red and blue shifted electromagnetic waves. The red-shifted component is amplified by the typical Brillouin relation.

As shown by Thompson⁽⁴⁾ this is slightly modified from the Forslund et al.⁽⁵⁾ expression but asymptotically approaches it for $t \geq L/2c_s$.

To briefly summarize our past results we have:

- (1) Quantitatively verified the predictions of Eq. (1) including the dependence on chamber reflectivity and v_0/v_{te} .
- (2) Observed the reflectivity from the ion acoustic fluctuations generated by the partially standing electromagnetic waves.
- (3) Verified frequency and wavenumber matching conditions.
- (4) Verified theoretical predictions for linear growth of reflectivity.⁽⁴⁾

- (5) Observed saturation of the reflectivity and associated density fluctuations.

During the past year we have continued to investigate the causes of the observed SBS saturation. Various models have been proposed to limit the growth of SBS. These include:

- (a) Ion Acoustic Harmonic Generation
- (b) Density Profile Modification
- (c) Ion Trapping
- (d) Ion Tail (or Main Body) Heating
- (e) Subharmonic Generation

As shown in Figs. 2 and 3, we do not observe any appreciable harmonic content either in the ion waves or the reflected power. We are therefore able to dismiss the first saturation mechanism. However, it is interesting to note that theory predicts^(6,7) that harmonic generation should occur for $(\bar{n}/n_0) > (k\lambda_D)^2$ which we greatly exceed. Furthermore, in a separate experiment where ion acoustic waves were launched by a grid we did observe harmonic generation. Work continues to resolve this apparent discrepancy.

The effects of density profile modification are easy to understand for the high intensity case. Kruer et al.⁽⁸⁾ showed that SBS is limited by the momentum and energy deposition associated with the reflection of the incident laser light. They demonstrated that large reflectivity could only occur on a timescale shorter than that required for the reflection front to travel through the underdense plasma. Although the reflectivity in our experiment is much lower than the value required for this effect to be appreciable, we do observe density profile modifications. Nevertheless, the magnitude of the modifications (=30-50%) is not sufficient to explain the observed saturation at =5% reflectivity.

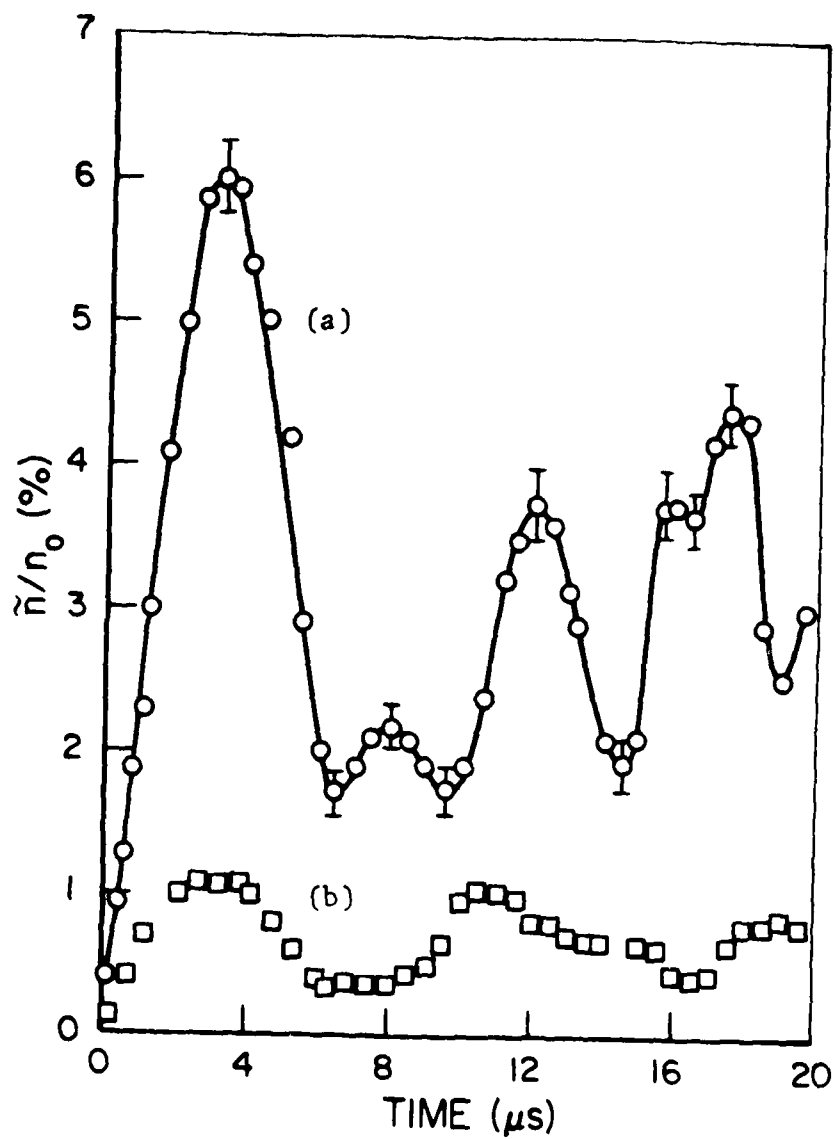
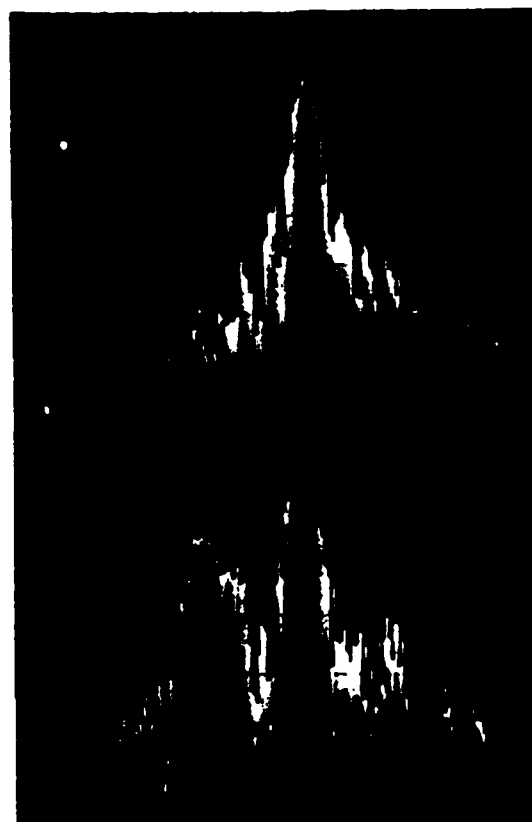


Fig. 2. Normalized Density Fluctuations as a Function of Incident Pulse Width. (a) H Plasma, $P_0 \approx 300$ kW, (b) He Plasma, $P_0 \approx 87$ kW.



Incident
Wave
400 kW

Reflected
Wave

↔
div

Center Frequency: 3.3 GHz
Horizontal Scale: 100 kHz/div
Vertical Scale : 5 dB/div

Fig. 3a Incident and Reflected Spectra
($H, \omega_s \tau = 23$ and $v_0/v_{\infty} = 0.67$).

Estimates of the effect of ion trapping have been made by Kruer.⁽⁶⁾ He finds that the limit in ion wave amplitude is given by

$$(\bar{n}/n_0)_{\max} = \frac{1}{2} \left[\left(1 + \frac{3\theta_1}{2\theta_e} \right)^{1/2} - \left(\frac{3\theta_1}{2\theta_e} \right)^{1/2} \right]^2$$

Inserting our experimental parameters we find $(\bar{n}/n_0)_{\max} = 19\%$. This predicts a saturation level approximately a factor of four larger than observed. In addition, energy analyzer measurements of the ion distribution function indicate that there is considerable tail heating rather than just simple trapping. Therefore, as we shall see, ion tail heating has proven to be the dominant saturation mechanism.

Before proceeding to a detailed discussion of the ion tail heating results, an additional mechanism somewhat peculiar to this experiment should be mentioned. Specifically, considerable electron main body heating occurs (up to a factor of 2-3) during the rf pulse and therefore v_0/v_{te} decreases with time. The heating mechanism is simply inverse Bremsstrahlung absorption where the collisions are primarily due to the neutral atom background. Although the heating is significant, it can easily be shown that the decrease in v_0/v_{te} should lead to a reduction in the reflectivity (over the linear prediction) rather than the observed saturation. As mentioned above, energy analyzer data have shown significant (10-20%) ion tail heating with a linear time dependency and some ion main body heating (50%). However, the low energy (main body) heating is somewhat suspect due to experimental difficulties with the analyzer. A curve fit of previous experimental work on the SRS reflectivity was obtained using measured density fluctuation levels and a linear ion tail heating rate, (Fig. 3(b) Solid Curve) fitting one point (300 kW) and extrapolating the rest of the curve. Excellent agreement resulted. However, we are concerned whether the actual dominant saturation

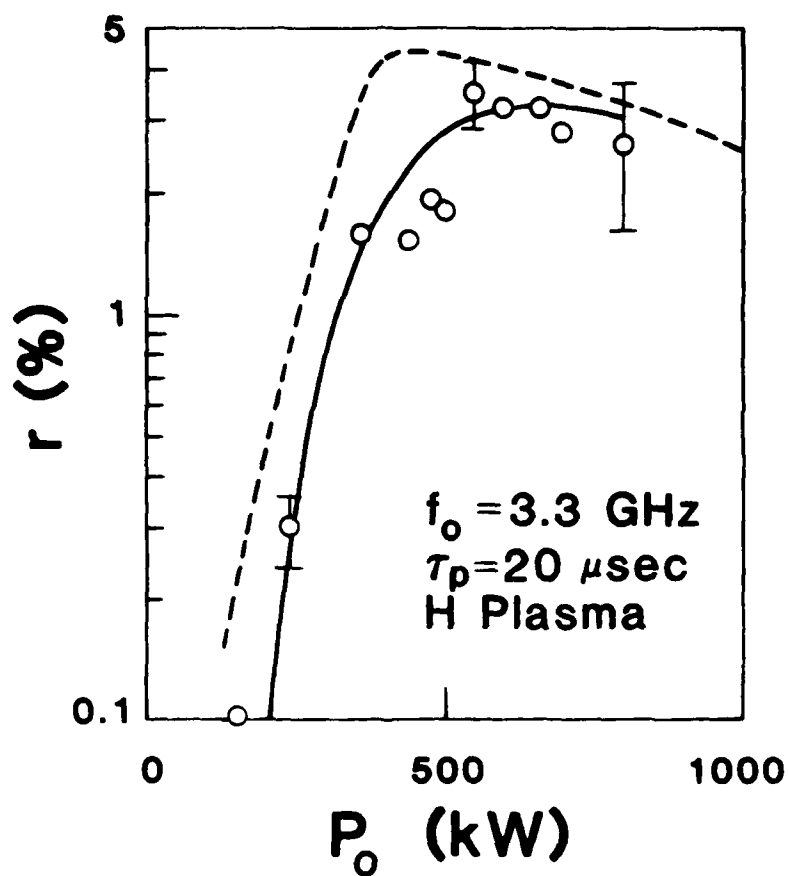


Fig. 3b Reflectivity Versus Incident Power
(Circles Experimental Results.)

mechanism is indeed main body ion heating or ion tail heating. The dotted line is a theoretical boundary limiting the maximum reflectivity to ion tail heating.

As mentioned above, energy analyzer data have shown significant ion tail heating ($\approx 10-20\%$) with a linear time dependence. Although some apparent ion main body heating has also been observed ($\approx 50\%$), experimental difficulties have thus far forced us to view these latter measurements with some suspicion. In addition, as discussed above, an excellent curve fit of previous experimental data on SBS reflectivity was made using the measured density fluctuation levels, the measured ion tail heating rate (at 300 kW), the electron heating rate and extrapolating the rest of the curve (see Fig. 3b). Since the experimental results could be fit so well without inclusion of the apparent ion main body heating we devoted considerable time both to improving the low energy performance of our energy analyzers as well as to performing detailed numerical calculation of the predicted reflectivity assuming various percentages of the incident energy (Manley-Rowe) deposited in the tail or the main body. Basically, a computer program was developed to calculate the SBS reflectivity and density fluctuation level, using the linear solution to the standing wave ponderomotive force initiated SBS theory developed by Thomson.⁽⁴⁾ A time dependence on T_e , T_i and n_{hot} was included. Electron heating is determined by inverse bremsstrahlung on the background neutrals. Ion main body heating is determined by equating the ion heating rate with the power deposited in the ion wave:

$$\frac{d}{dt} (n_o T_i) = R \frac{P_o}{A l} \frac{\omega_s}{\omega_o}$$

The hot ion tail is determined by equating that power with the hot tail free-streaming energy flow^(6,7) yielding

$$\frac{1}{2} (n_h M c_s^2) c_s = R \frac{P_o}{AL} \frac{\omega_s}{\omega_o}$$

In brief, it was seen that the ion main body heating case predicted behavior completely opposite that observed experimentally. On the other hand, the ion tail heating case predicts behavior identical to that observed experimentally. A typical case is shown in Fig. 4. In addition, as we will see in the next section, the optical mixing results also show that ion tail heating is the observed mechanism.

Finally, we note that recently we have made some preliminary measurements with increased wall reflection which appear to show some rescatter. As shown in Fig. 5 above a certain power level harmonics are observed in the red-shifted side of the microwave spectrum. Work continues at identifying the mechanism.

B. OPTICAL MIXING GENERATION OF SBS WAVES

As discussed in the preceding section, our microwave SBS simulations were limited (by the low ionization percentage of the target plasma) to short to moderate duration pulses on the ion timescale. In addition, bremsstrahlung absorption on the neutrals caused v_o/v_{te} to change during SBS growth complicating our interpretation of the primary saturation mechanism (ion tail heating). To improve the experimental conditions, we decided to employ optical mixing to study the growth and saturation of the SBS ion waves. By driving both of the SBS electromagnetic waves (with the proper frequency shift) we obtain ion fluctuations of comparable amplitude to the "pure" SBS case at considerably lower rf power levels (1-2 orders of magnitude). As we will see in the following, this permits us to look at phenomena on much longer timescales ($\omega_s \tau_p \leq 10^4$). In addition, the reduced power levels result in

REF94.88S

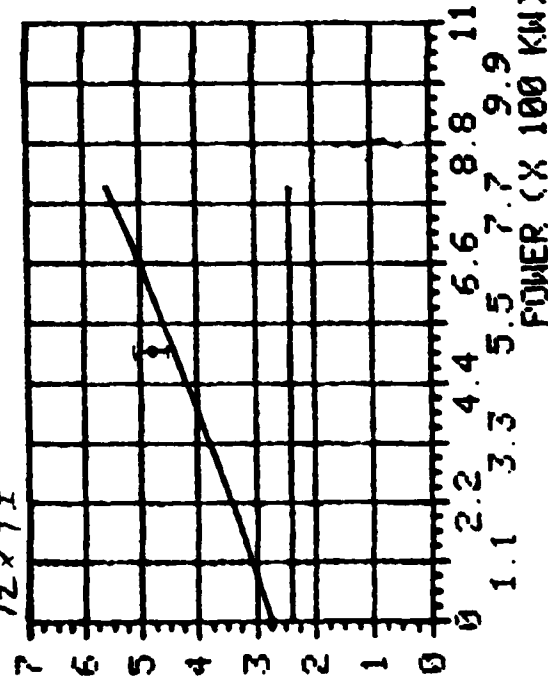
$N\phi - 0.1 N_c$

TIME: 19.96 USEC

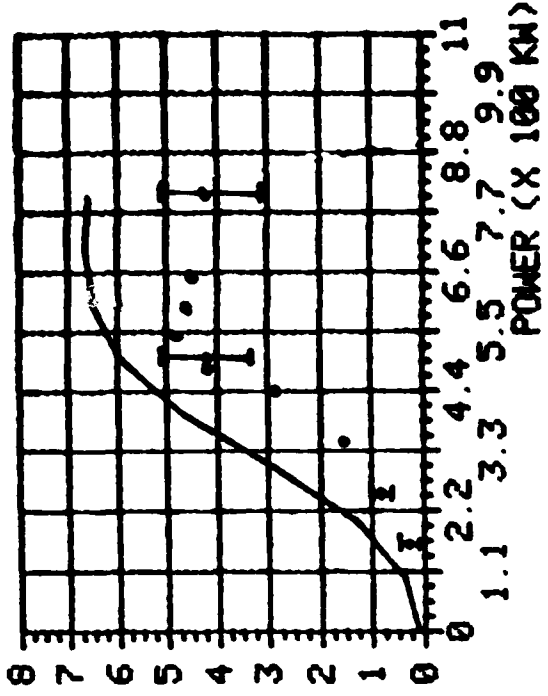
$1E-3 N/N_c$

TE (eV)

$12 \times T_I$



1E-3 R-THOMSON



$1E-3 N-HOT / N_c$

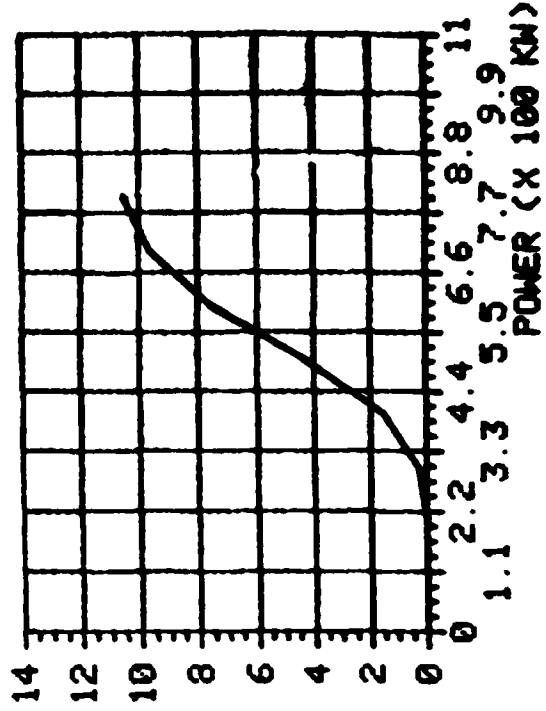
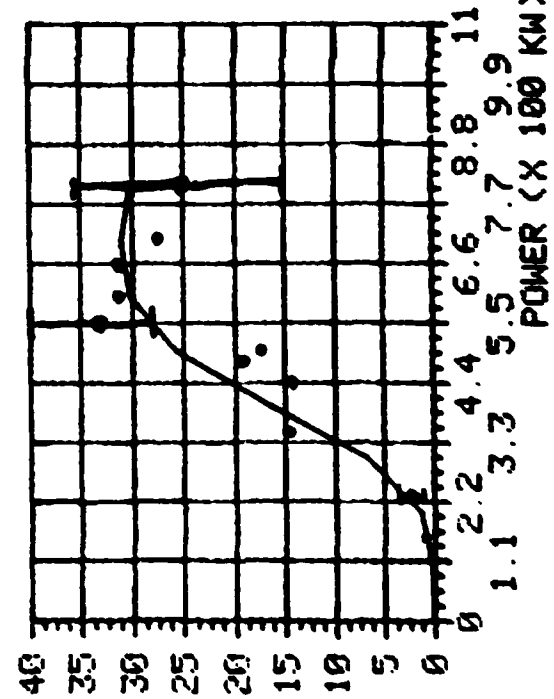


Figure 4 Comparison of Measured Electron Temperature, Density Fluctuation Level and Reflectivity with Numerical Predictions for Various Power Levels.

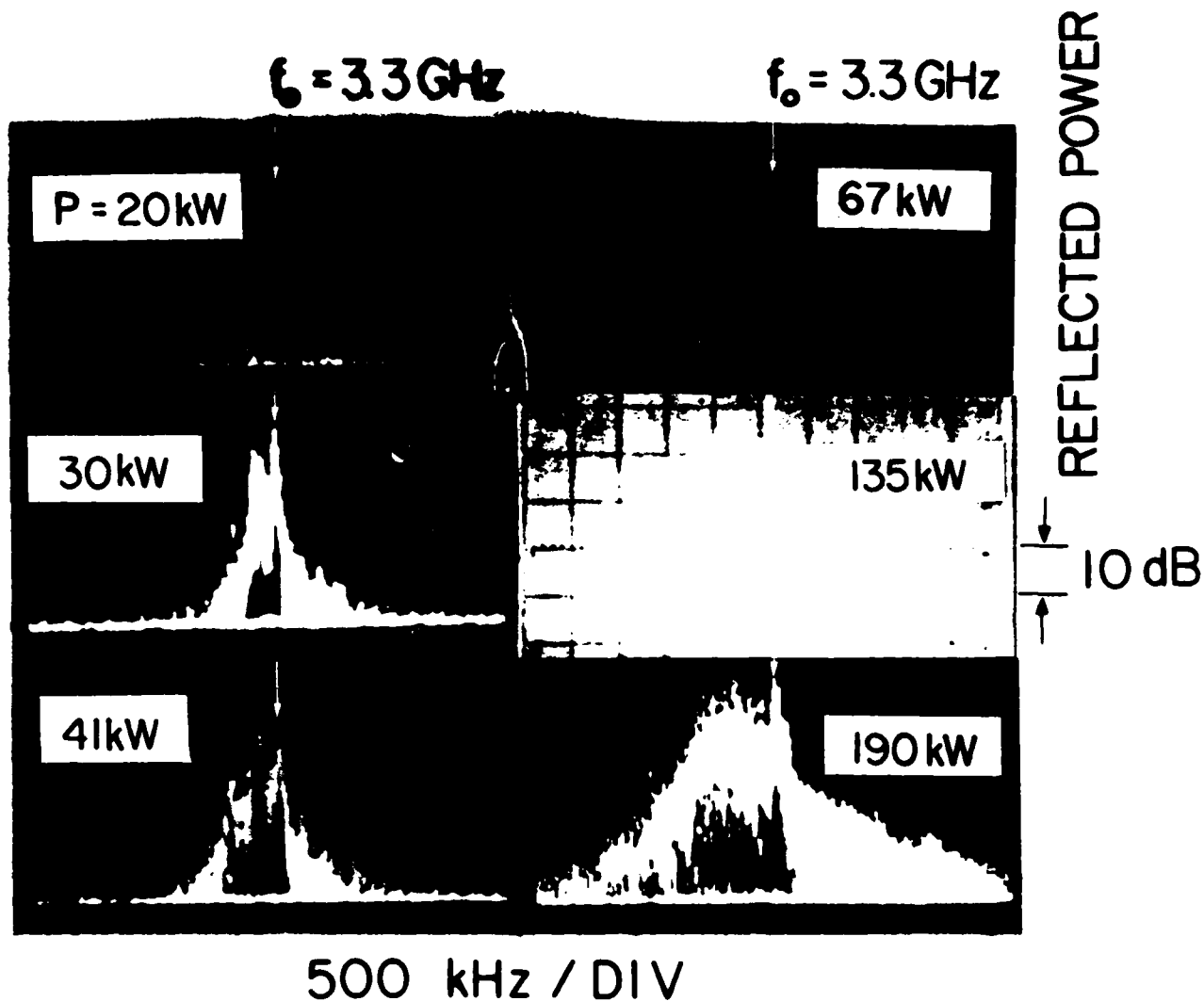


Fig. 5 Power Spectrum of Reflected Light for Various Input Power Levels for Case of Increased Wall Reflectivity.

negligible profile modifications or electron heating permitting us to clearly focus on the ion heating saturation mechanism. Interestingly, the saturation level, etc. is identical to the SBS case described in Sec. IIA.

Before discussing the optical mixing experimental results, let us briefly review the linear predictions. Consider two electromagnetic waves propagating in the \hat{x} -direction with

$$E_1 = \hat{x} E_1 e^{ik_1 x + i\omega_1 t}$$

and

$$E_2 = \hat{x} E_2 e^{-ik_2 x + i\omega_2 t}$$

The pondermotive force

$$F_{NL} = -\frac{\omega^2}{\omega^2} \frac{\nabla \langle E^2 \rangle}{8\pi}$$

For our case, the relevant term is

$$\langle E^2 \rangle = 2E_1 E_2 \cos[(k_1 + k_2)x + (\omega_1 - \omega_2)t]$$

We obviously expect a large response when

$$\frac{\omega_1 - \omega_2}{k_1 + k_2} = v_{ph}$$

for the ion acoustic wave.

The linear theory predicts that the collision limited amplitude (time asymptotic steady oscillation amplitude) is given by

$$\bar{n}/n_0 = \frac{e^2 E_1 E_2}{m^2 \omega_1 \omega_2} \left(\frac{n}{2M}\right) \frac{k_s^2}{\nu_{ion} \omega_s}$$

$$= \frac{v_1 v_2}{v_{te}^2} \left(\frac{n}{2M}\right) \frac{k_s^2 v_{te}^2}{\nu_{ion} \omega_s}$$

This yields $\bar{n}/n_0 = 0(1)$ for $v_{1,2}/v_{te} = 0.2$ or for $P = 50$ kW. We therefore expect to reach nonlinear saturation at extremely low powers compared to the pure SES case. The linear time dependent prediction for the ion wave growth is

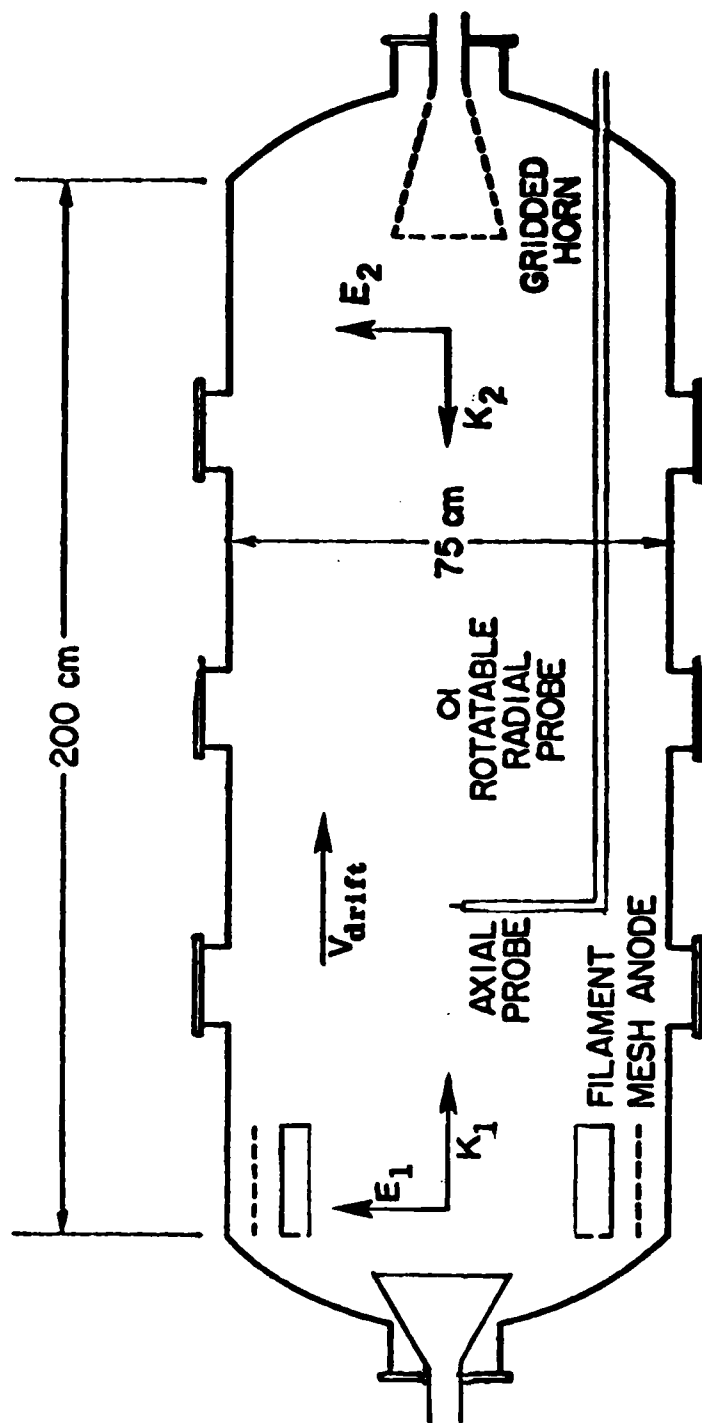
$$\bar{n} = F_{NL} e^{\frac{-1}{2} \frac{\nu_{ion}}{\omega_s} (t-\tau)} \left(e^{\frac{-\nu_{ion}\tau}{2}} - 1 \right) \frac{e^{-i\omega_s \tau}}{1 - \nu_{ion} \omega_s}$$

where τ is the rf pulse duration and $t > \tau$. Again we predict large density fluctuation levels at moderate power levels even for microsecond duration pulses.

To perform the experimental studies, a second horn was added to the SBS chamber as shown in Fig. 6. The most difficult problem was maintaining the frequency stability of the two rf sources. Specifically, since $\omega_s/2\pi \approx 200$ kHz and $\omega_{1,2}/2\pi \approx 3$ GHz this placed a severe constraint on the system. However, using frequency synthesizers and frequency multipliers followed by amplifiers we were able to obtain a system with 150 Hz stability (≈ 1 part in 10^7) where the difference frequency between the two sources could be varied continuously from zero to arbitrarily large values.

As will be briefly shown, the experiments have been extremely successful. The results are presently being written up for journal submittal.

First, let us examine the evidence for the existence of optical mixing. As shown in Fig. 7, a large ion wave is produced for moderate power levels (≈ 20 kW). Figure 8 demonstrates that the large ion response is only produced when the separation frequency between the rf sources corresponds to the proper ion



H, He, Ne, Ar, Kr

$p = (1-3) \times 10^{-4}$ Torr

$T_e \approx 2$ eV

$T_e/T_i \approx 10-12$

$L_n \cdot L_T \gtrsim 2$ m

$n_0 \approx 0.1$ nor

Fig. 6 Experimental Arrangement for Optical Mixing.

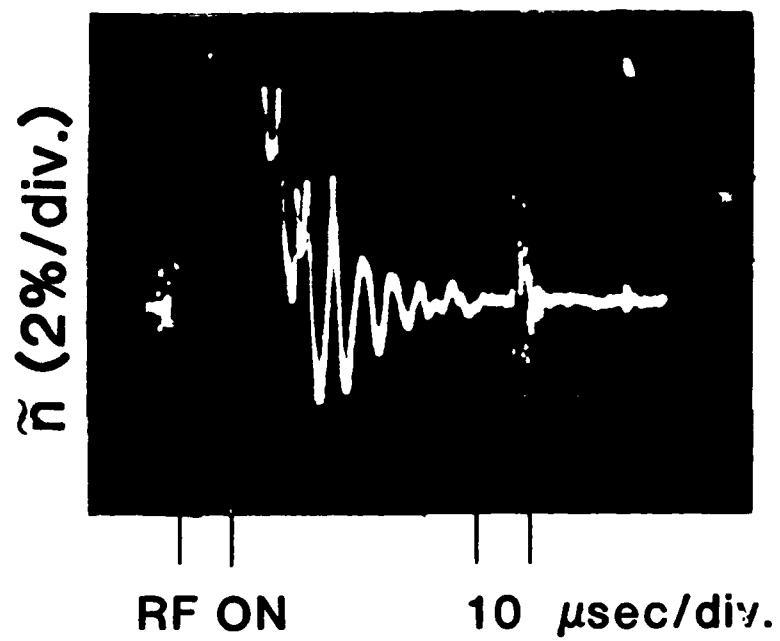


Fig. 7 Ion Waves Generated by Optical Mixing.

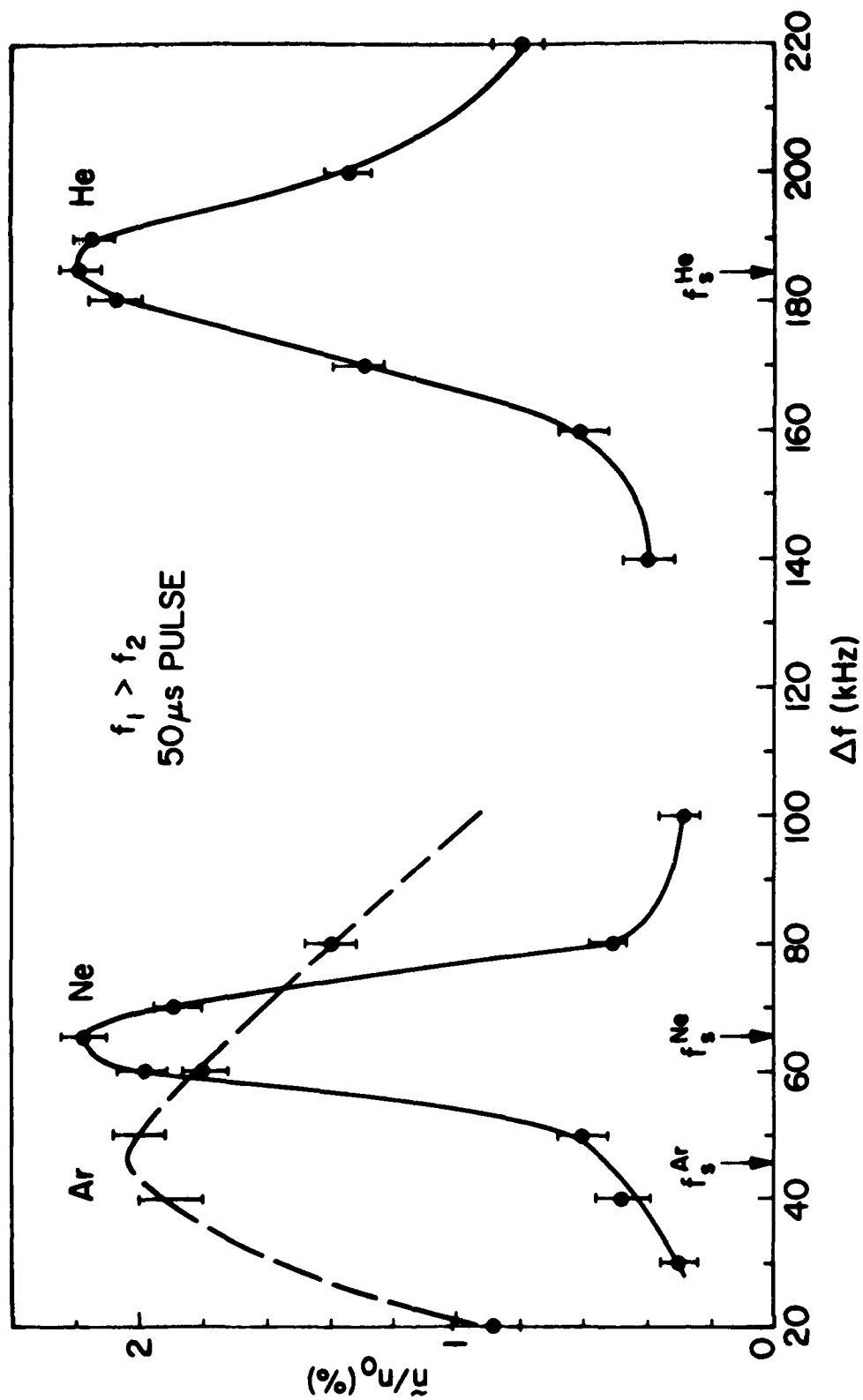


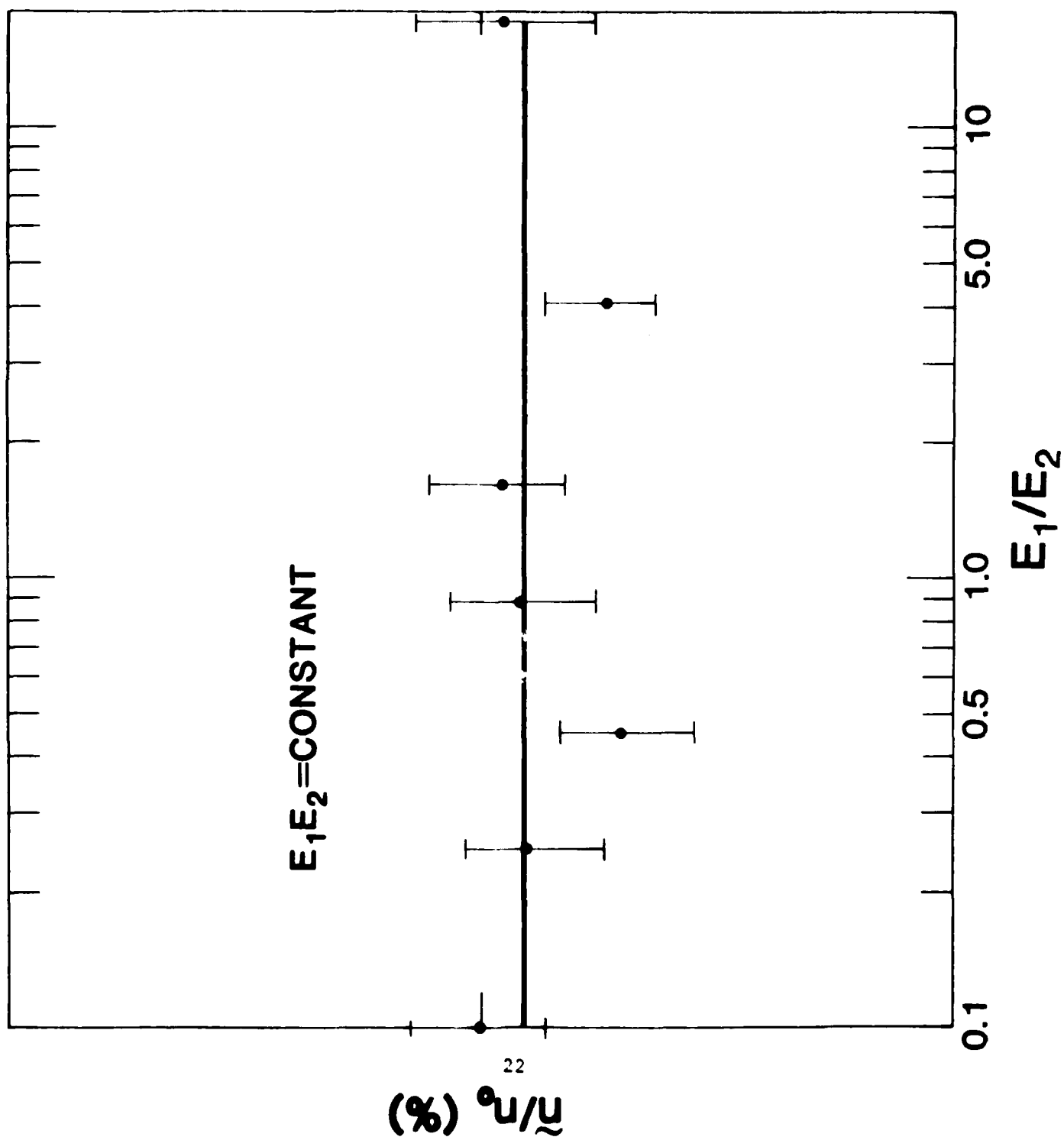
Fig. 3 Density Fluctuation Level as a Function of Difference Frequency of rf Sources.

acoustic frequency for the ion species employed. As shown earlier, the density fluctuation levels should depend only on the product $E_1 E_2$ and not the actual ratio E_1/E_2 . As shown in Fig. 9 this dependence is in fact observed. Here $E_1 E_2$ was held constant and E_1/E_2 varied by two orders of magnitude. Further confirmation of this scaling is shown in Fig. 10. Here we see that $(\bar{n}/n_0)_{\max}$ scales linearly with $E_1 E_2$ up to saturation. It is interesting to note that the saturation level is identical to that observed in the SBS studies. Having conclusively identified the linear predictions of the optical mixing theory we then set out to investigate the nonlinear saturation.

As shown in Fig. 11, the saturation level appears to be independent of the pulse duration. As long as the power level is sufficiently high to reach saturation (as opposed to the simple linear collisional steady-state) one simply must employ longer pulse durations to reach saturation as the incident power is reduced. This point is illustrated in more detail in Fig. 12. Here we see that for $P \geq 15$ kW, we reach nonlinear saturation whereas for 9 kW we arrive at the collisional steady-state oscillation amplitude at a lower level.

The saturation mechanism was studied in detail. First, we verified that for the optical mixing power levels there was virtually no change in electron temperature ($v_0/v_{te} = \text{constant}$) and no profile modifications. However, as shown by the energy analyzer results of Fig. 13, there is a significant heating of the ion distribution in the presence of the rf. Figure 14 shows the increase in the fraction of ions with energy greater than 1.5 eV ($T_{i0} = 0.2$ eV) with increasing $E_1 E_2$. The resonant nature of the heating is clearly seen in Fig. 15; the heating only occurs when $|\omega_1 - \omega_2| = \omega_s$. Recently, we have performed numerical calculations which demonstrate that the measured ion heating is sufficient to completely account for the observed saturation. In this model we calculate in each step the work done by the optical mixing on

Fig. 9 Density Fluctuation Level as a Function of E_1/E_2 with E_1E_2 Held Constant.



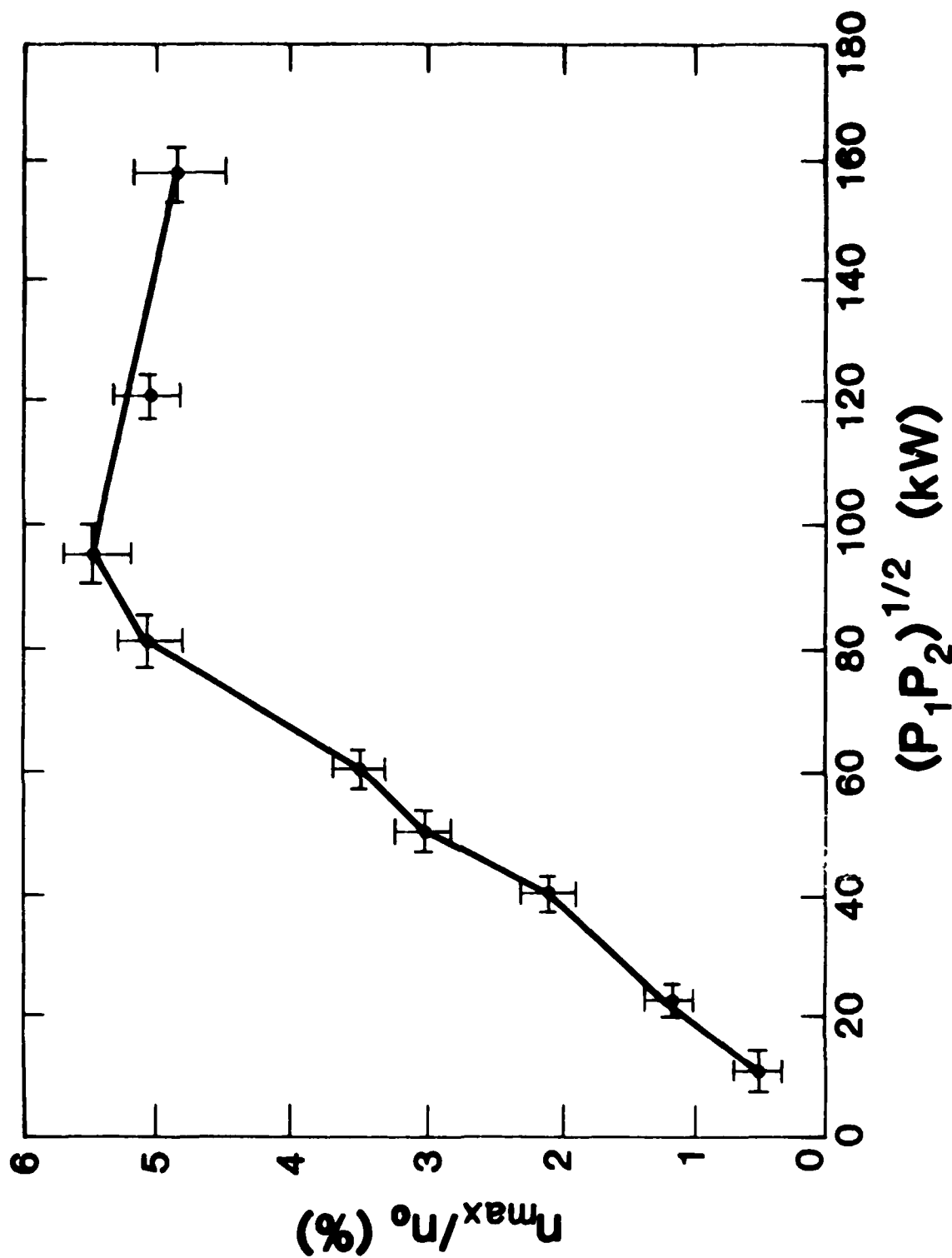


Fig. 10 Peak Density Fluctuation Level as a Function of $\varepsilon_1 \varepsilon_2 = (P_1 P_2)^{1/2}$.

N/No

Computer model curves and data points

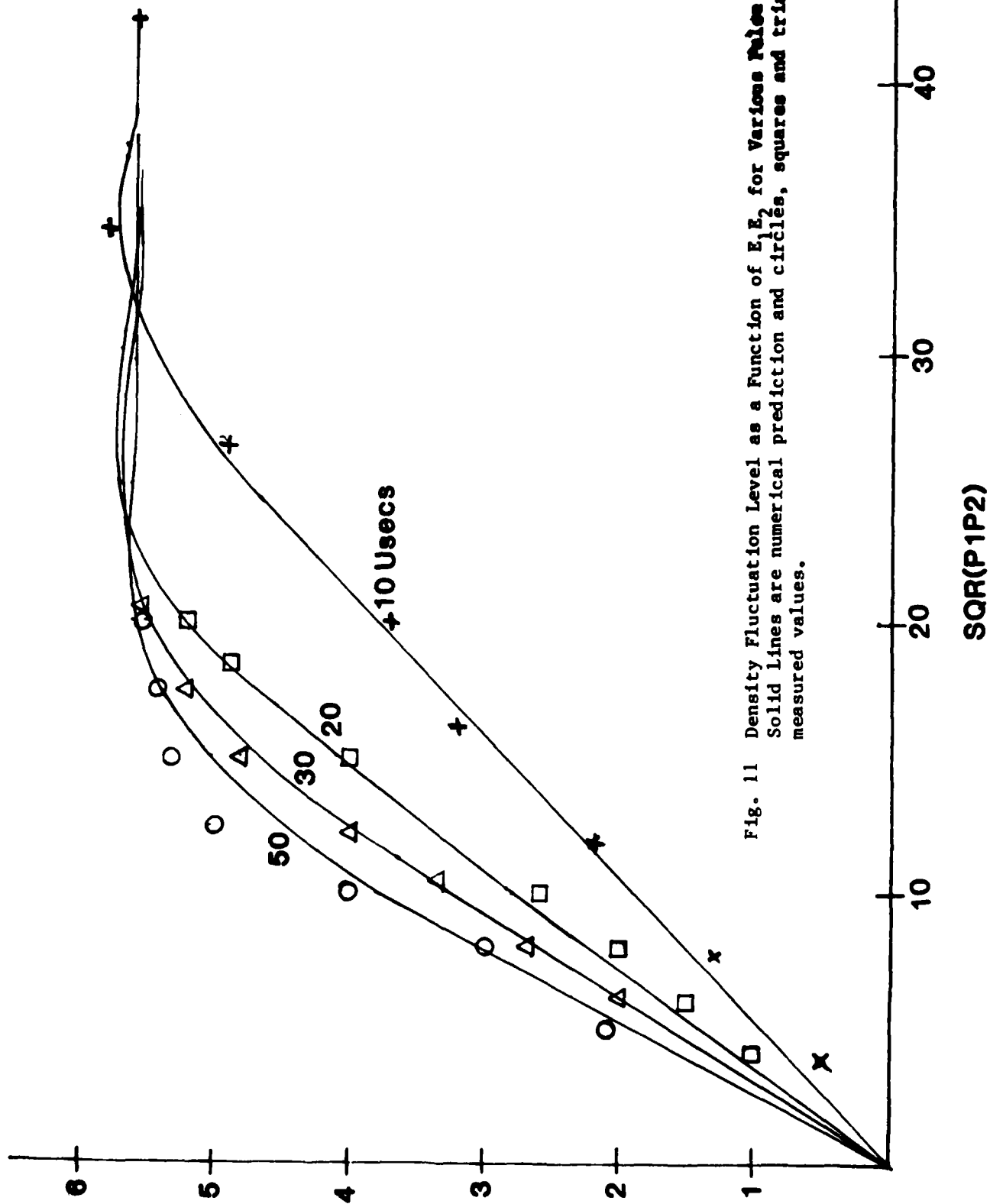


Fig. 11 Density Fluctuation Level as a Function of E_{12} for Various Pulse Durations: Solid lines are numerical prediction and circles, squares and triangles are measured values.

N/No

Curves are generated by the computer program described.
corresponding data points are plotted

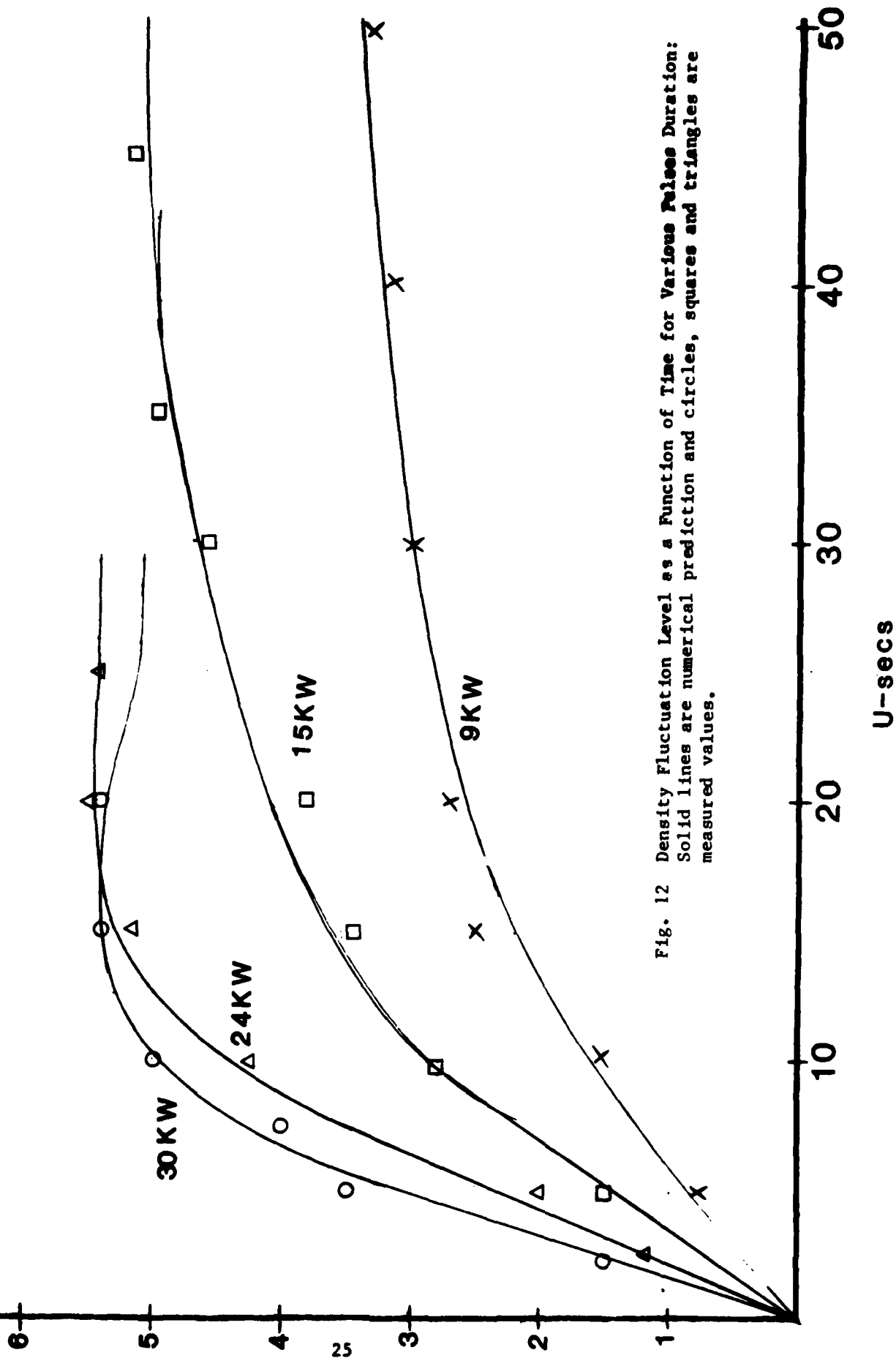


Fig. 12 Density Fluctuation Level as a Function of Time for Various Pulse Duration:
Solid lines are numerical prediction and circles, squares and triangles are measured values.

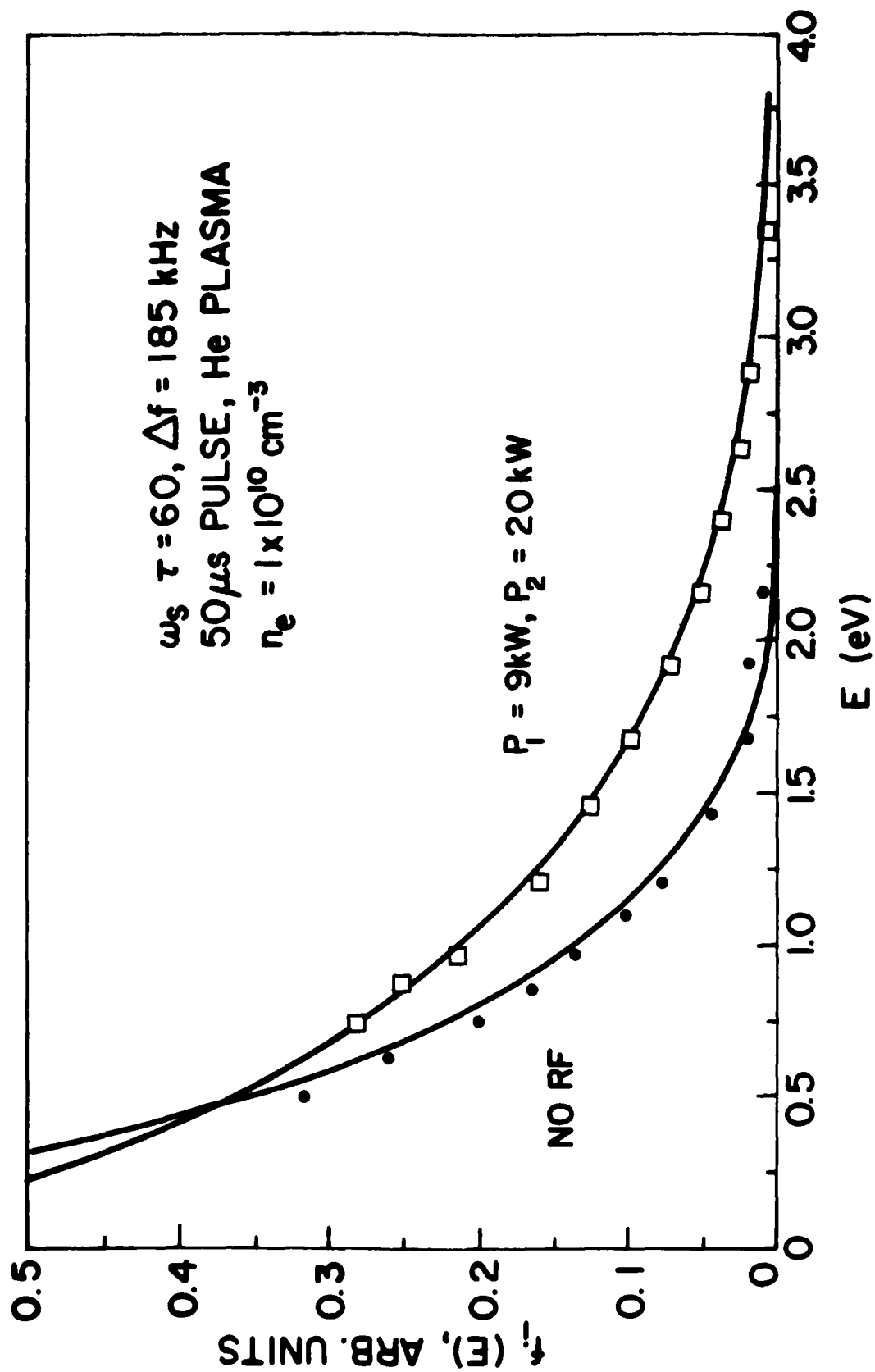


Fig. 13 Ion Tail Distribution Function with and without rf.

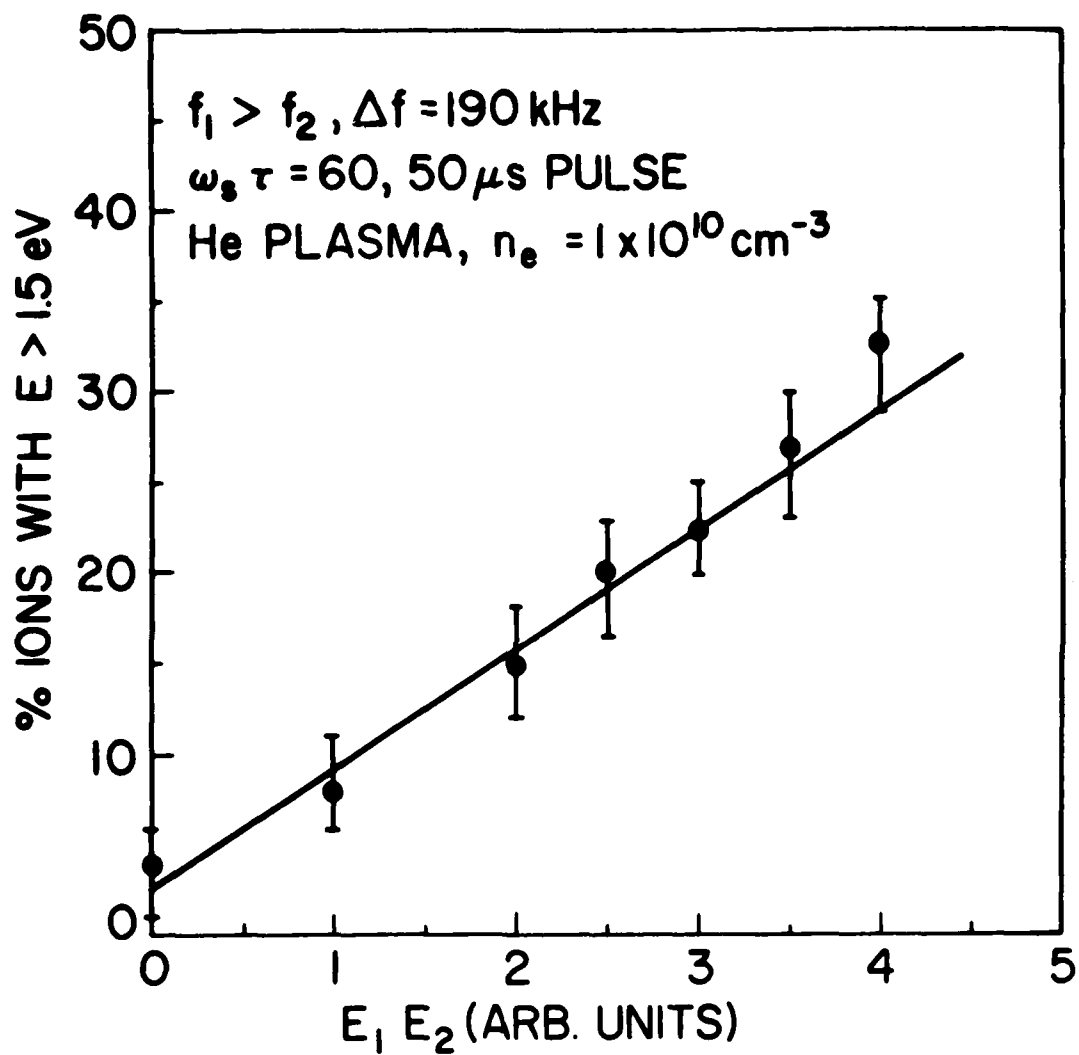


Fig. 14 Fraction of ions with Energy Greater than 1.5eV ($\approx 5KT_1$) as a Function of $E_1 E_2$.

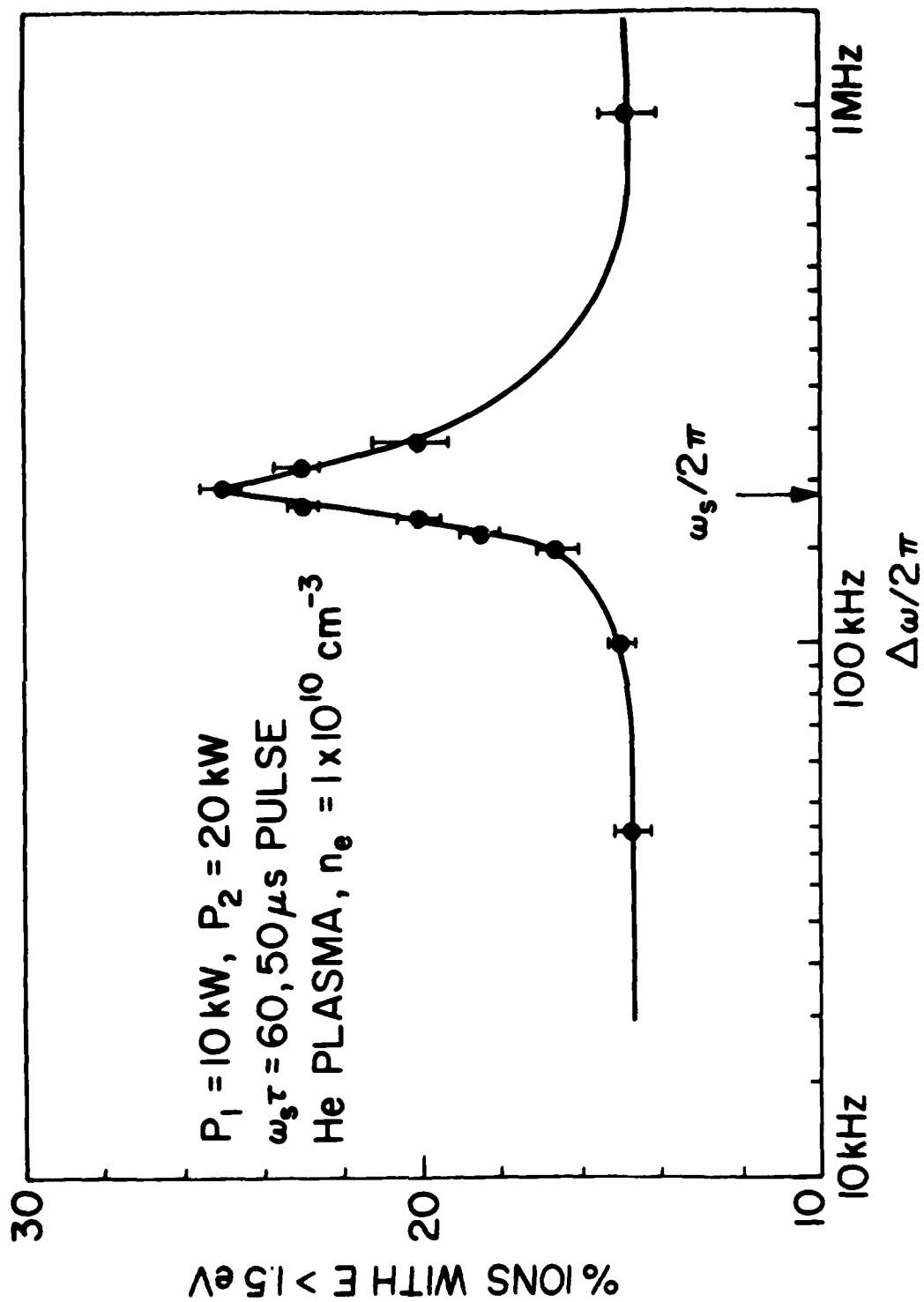
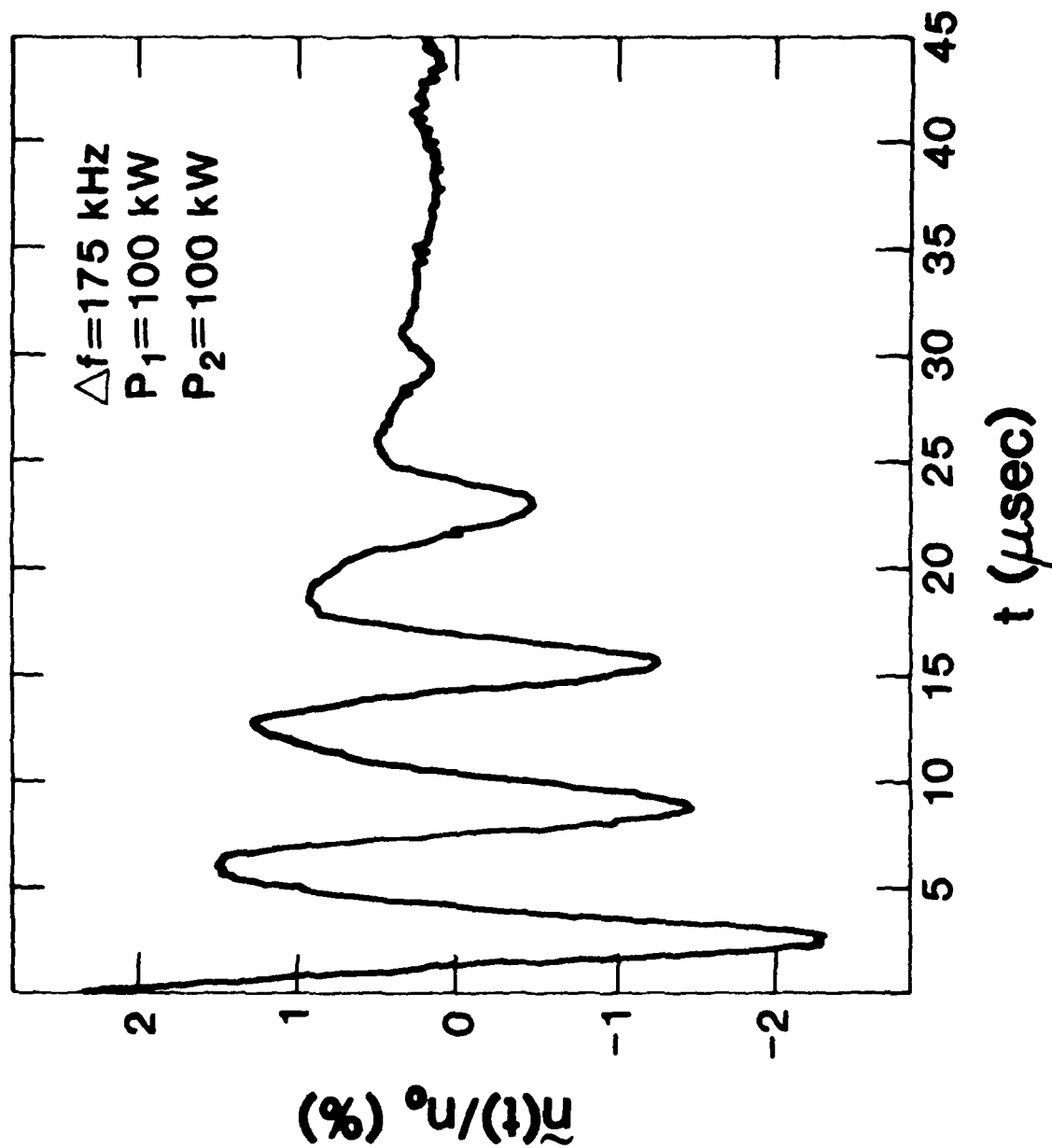


Fig. 15 Fraction of ions with Energy Greater than 1.5eV as a Function of the rf Source Difference Frequency.

the ion distribution assuming that it goes into the tail. We then calculate the total damping (collisional and Landau) and repeat the calculation on each time step. As shown in Figs. 11 and 12 the agreement between experiment and the model's prediction is quite good.

At this point it should be mentioned that there still remain some unresolved mysteries. First, the question of why we sometimes see ion wave harmonics has not been answered. In the optical mixing studies the harmonics appear to depend sensitively on the wall reflections. Figure 16 shows the coherent ion wave produced under conditions where there are appreciable chamber wall reflections present (equivalent to four electromagnetic waves). The ion wave harmonic content is seen to be negligible. On the other hand, the results shown in Fig. 17 correspond to the case where the chamber wall reflections were greatly reduced. A second puzzle concerns the effect of introducing a light ion impurity on increasing the damping and consequently decreasing the fluctuation level. As shown in Fig. 18 adding a He impurity to a Ne plasma does in fact decrease the amplitude of the optical mixing generated ion wave. Here the actual damping rate was measured by observing the decay of the ion wave after rf turn-off. The mystery is that the decrease was too large to be explained by the observed damping. The first thought that comes to mind is that the impurity also shifts the ion frequency and that since the frequency was maintained constant the decrease is due to the off-resonance drive condition. However, calculations of the expected frequency shift indicate that this is a small effect. We are therefore investigating the possibility that the damping is anomalously high. Work continues on understanding both of these puzzles.

Fig. 16 Ion Wave Time History After rf Turn Off for Case Without Absorber on Chamber Sidewall.



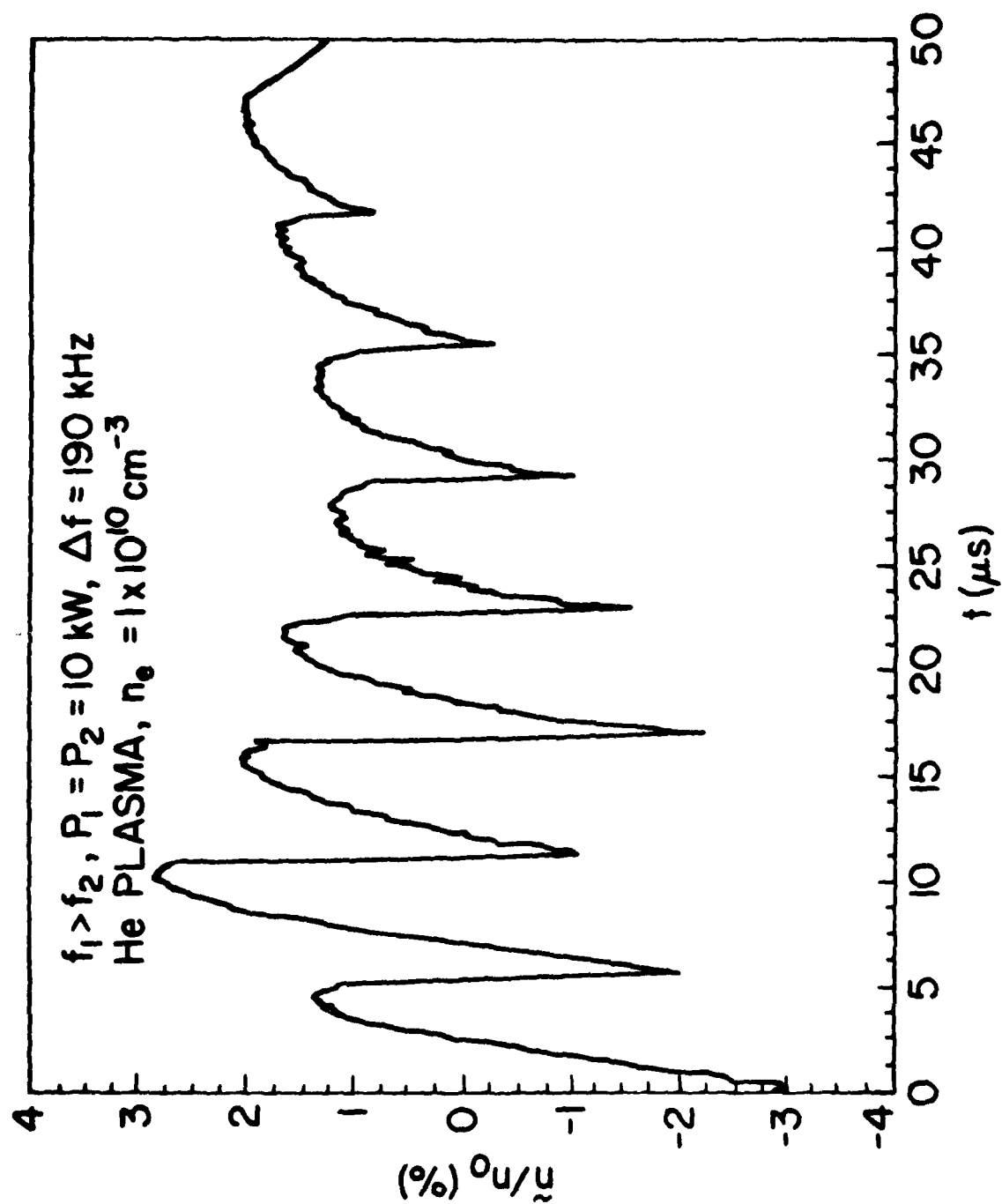


Fig. 17 Ion Wave Time History for Case with Absorber on Chamber Sidewall.

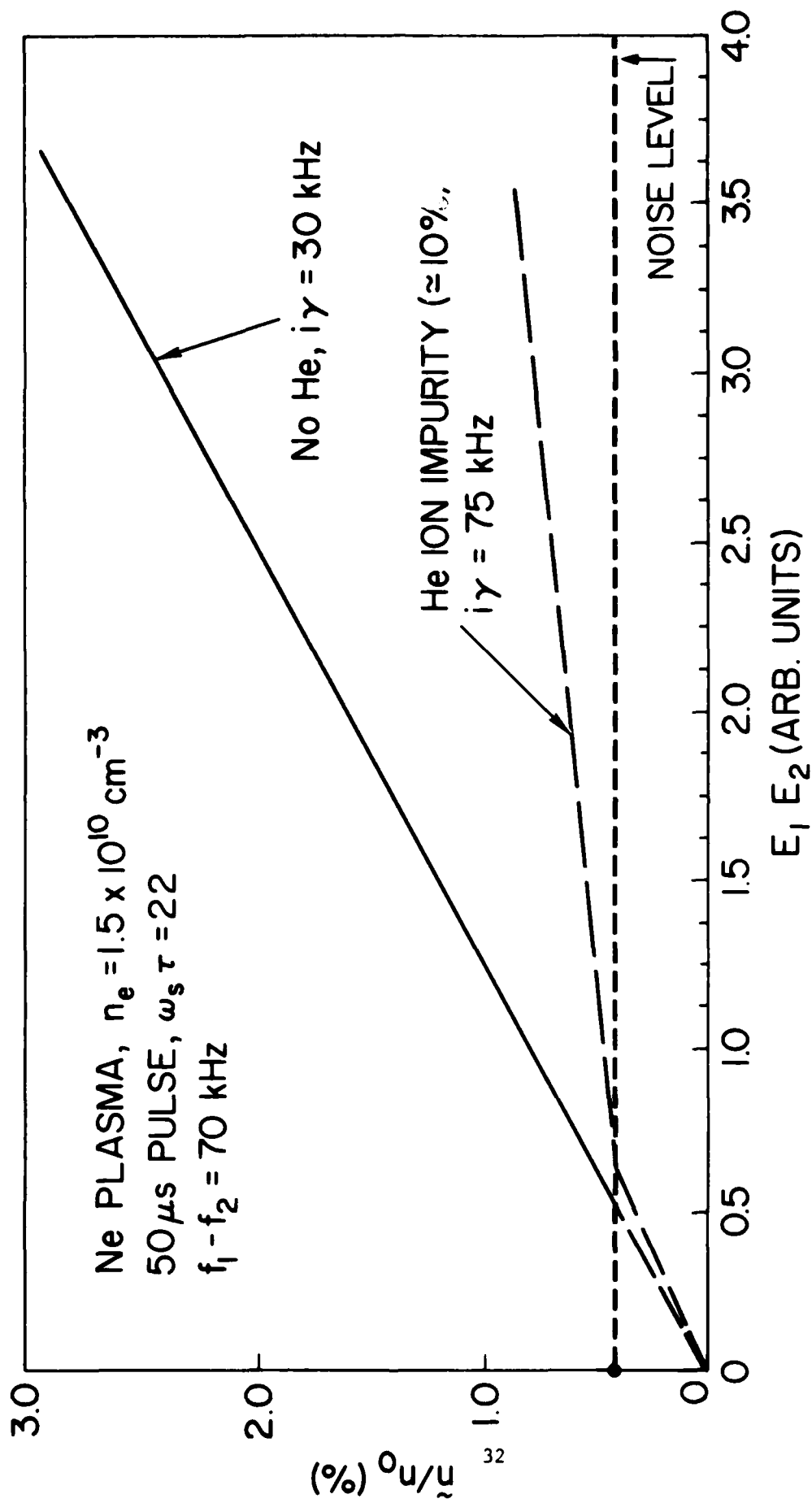


Fig. 18 Ion Wave Amplitude versus $E_1 E_2$ for Cases With and Without Light ion Damping,

C. RESONANCE ABSORPTION STUDIES

Our efforts during the past fiscal year have been devoted toward the initial value problem ($\omega_{pe} \tau \leq 10^4$) of the growth and saturation of resonance absorption produced electric fields and the associated hot electrons. Specific attention has been paid to the effect of a finite bandwidth pump on these phenomena. Here we were fortunate in that there are available both analytic models ^(9,10) as well as computer ⁽¹¹⁾ results with which to compare our experimental data. The results of this work are briefly summarized in this section.

The experiments were performed in the apparatus shown in Fig. 19. Microwave radiation ($\omega_0/2\pi = 3$ GHz) is launched along the axis of an inhomogeneous plasma ($L_n/\lambda_0 = 5$, $T_e/T_i = 10$). Movable electric and magnetic probes and energy analyzers permit the study of the resonance absorption produced fields and the associated hot electrons. The incident power level was kept small enough ($3 \times 10^{-6} \leq \eta_0 = E_{vac}^2/8\pi nKT_e \leq 3 \times 10^{-3}$) and the rf pulse durations short enough ($\omega_{pe} \tau \leq 10^4$) that density profile modifications were minimized ($\bar{n}/n_0 \leq 14\%$). These experimental conditions were chosen so that comparisons with fixed profile initial value saturation calculations of resonance absorption could be made.

As shown in Fig. 20, the electrostatic field in the vicinity of the critical layer grows rapidly and then saturates. Associated with the electric field growth is the production of hot electrons. In addition, finite bandwidth is seen to clearly reduce the electric field amplitude as well as the hot electron growth. During the past year we have continued our studies aimed at an understanding of these phenomena. This work has paid off and we now appear to have a fairly complete picture of the interaction.

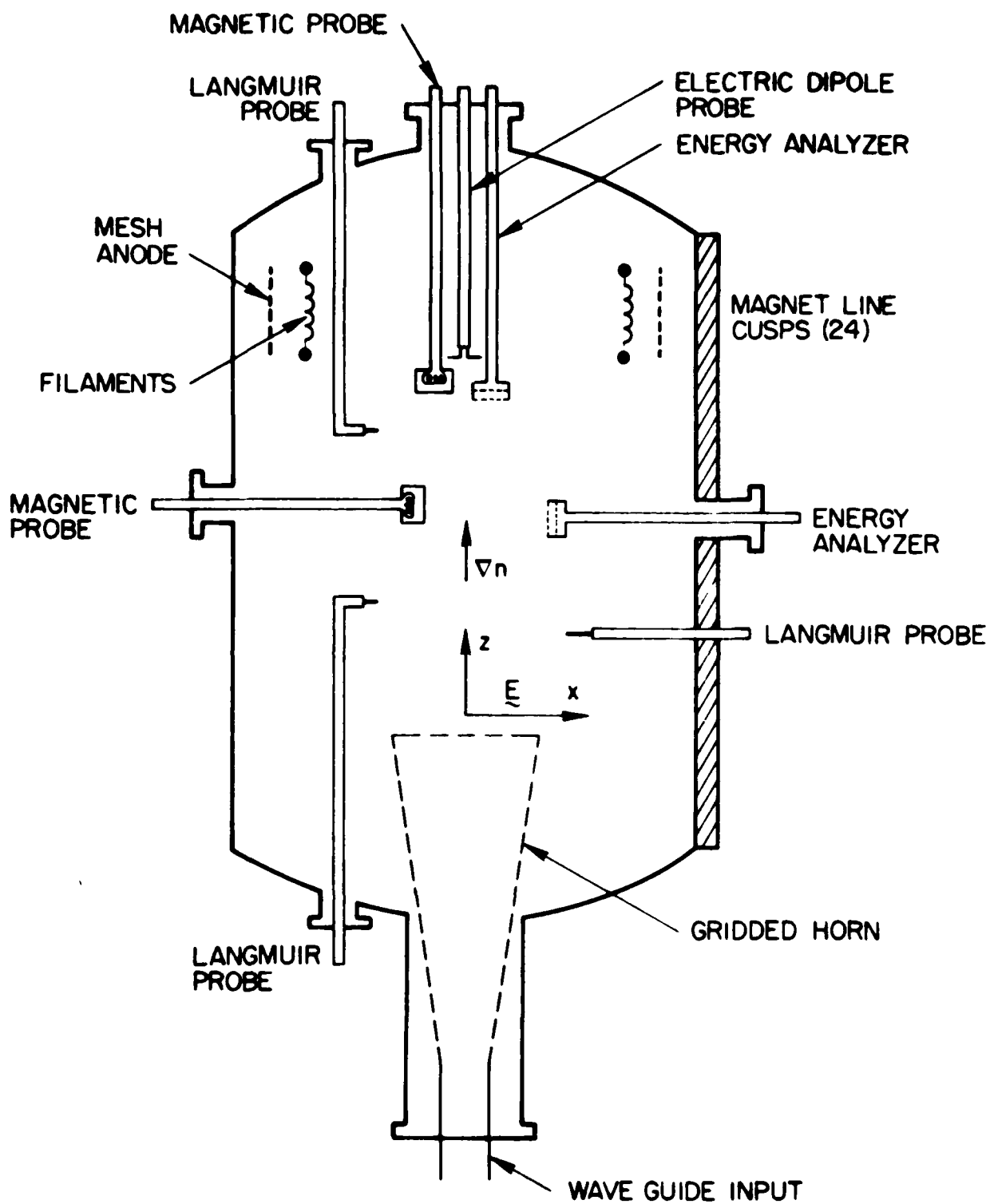


Fig. 19 Experimental Arrangement for the Investigation of Resonance Absorption.

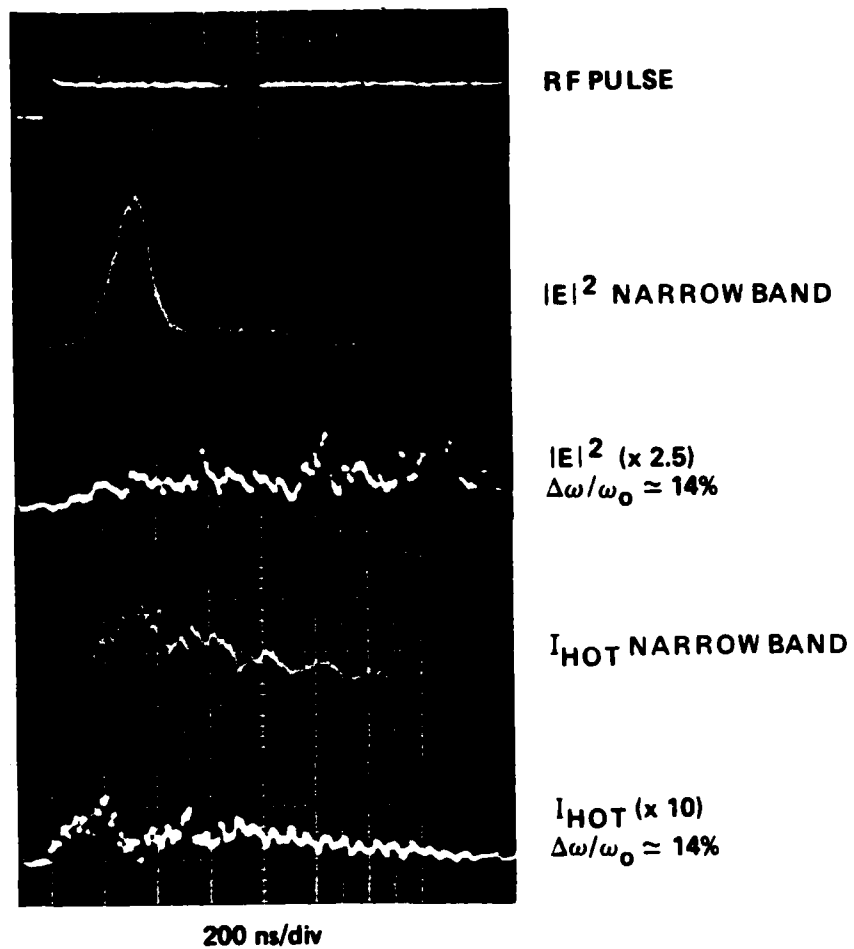


Fig. 20 Time History of Incident rf, Electric Field Intensity Near the Critical Layer and Hot Electron Current.

Let us begin first with the narrowband results. There are two commonly mentioned saturation mechanisms which limit the amplitude of the resonance absorption fields. These are convective saturation and cold plasma wavebreaking saturation. They give rise to predicted values for the saturated electric field of

$$E_c = 1.25 E_d (\omega_0 L / v_{te})^{2/3}$$

and

$$E_b = E_d (2Lm\omega_0^2 / eE_d)^{1/2}$$

respectively. Here $E_d = E_0 \phi(\tau) / (2\pi k_0 L)^{1/2}$ where E_0 is the vacuum electric field strength and $\phi(\tau)$ is the resonance function with $\tau = (k_0 L)^{1/3} \sin\theta$. Commonly, one calculates the magnitude of these for his experimental parameters and takes the one which yields the smaller number as the saturation mechanism. However, as we have shown this year, this prescription can lead to significant errors. As indicated in Fig. 21, convective saturation is expected to dominate for power levels up to 20 kW. However, experimentally we find that only for power levels < 1 W do we observe pure convective saturation. A complete transition to cold plasma wavebreaking saturation occurs at $P = 50$ W ($eE_{es} / m\omega v_{te} \approx 1$). The explanation for the large discrepancy appears to reside partially in the fact that the simple warm fluid picture is inapplicable when the quiver velocity exceeds v_{te} and also the fact that small density profile modifications can lead to a reduction in the effective loss rate of the electron plasma waves. Computer simulations are currently being done by C. Randal of LLNL⁽¹²⁾ for our experimental parameters and may shed additional light on this point.

The regime in which the saturation appears to be due to cold plasma wavebreaking was investigated in great detail. Specifically, we showed that the saturated electric field scaled with the incident power as $P^{0.5}$ as

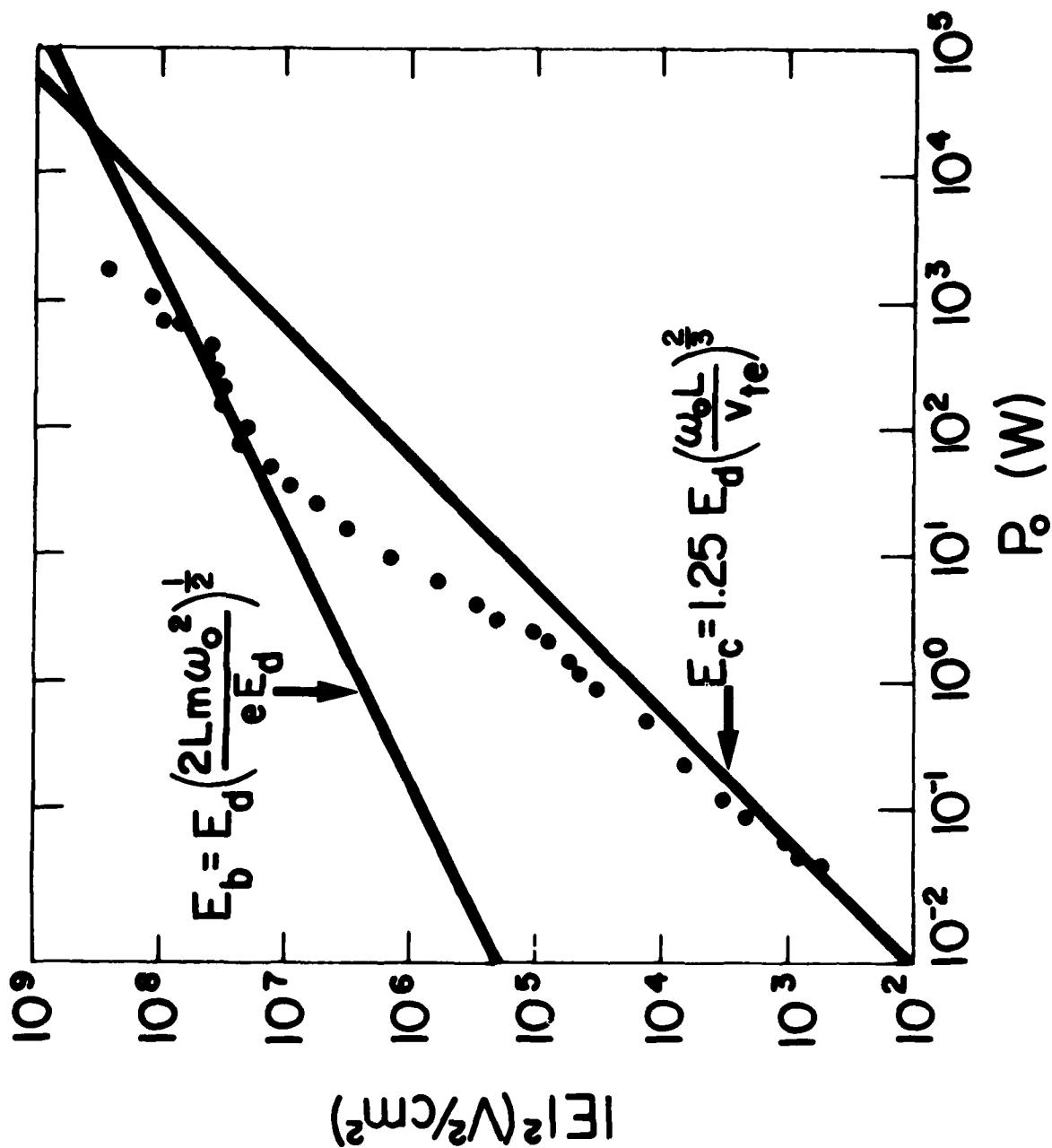


Fig. 21 Electric Field Intensity Near the Critical Layer versus Incident Power: Solid lines are theoretical predictions for wavebreaking and convective saturation. Data is fit to the wavebreaking curve at $P_0 = 213\text{W}$.

predicted. In addition, the wavebreaking time $t_b \propto P^{0.25}$ and had close quantitative agreement with the predicted time. As shown earlier in Fig. 21 hot electron production is associated with the growth of the resonance absorption produced fields. As shown in Fig. 22 the hot electron spectrum shows clear indications of its wavebreaking nature. Here the hot electron current detected by an energy analyzer is shown as a function of analyzing voltage. The formation of a hot electron tail is clearly seen as well as a cutoff energy $\bar{\epsilon}_m$ above which the hot electron density drops rapidly. It was found that $\bar{\epsilon}_m \propto P^{0.5}$ in good agreement with the predicted $P^{0.5}$ scaling. In addition, experiments showed that $T_h \propto P^{0.6}$. A further point to note is that finite bandwidth significantly reduces both $\bar{\epsilon}_m$ and T_h . This will be discussed in more detail later in this section.

As the amplitude of the electron oscillations increase during the approach to wavebreaking, strong harmonic content in their velocity and associated electric field spectra is anticipated. We therefore set out to look for such harmonic content as part of our identification process. Figure 23 shows the time histories of the total electric field intensity together with that of the second and third harmonics. We see that the peaks coincide but that the growth of the harmonics is delayed as expected until the waves nonlinearly steepen. Figure 24 shows that the wavebreaking time and electric field amplitude of the second harmonic also scale properly with incident power. The ratio of the various harmonics of the electric field intensity is easily calculated.⁽³⁾ Specifically, one expects that below wavebreaking the maximum intensities scale as

$$E_{(m)}^2/E_{(p)}^2 = p^2 J_m^2(m\alpha(t)) / m^2 J_p^2(p\alpha(t))$$

where m and p are the harmonic numbers, $\alpha(t) = 2\Delta \sin^2(\omega_{pe} \tau/2)$ with Δ the

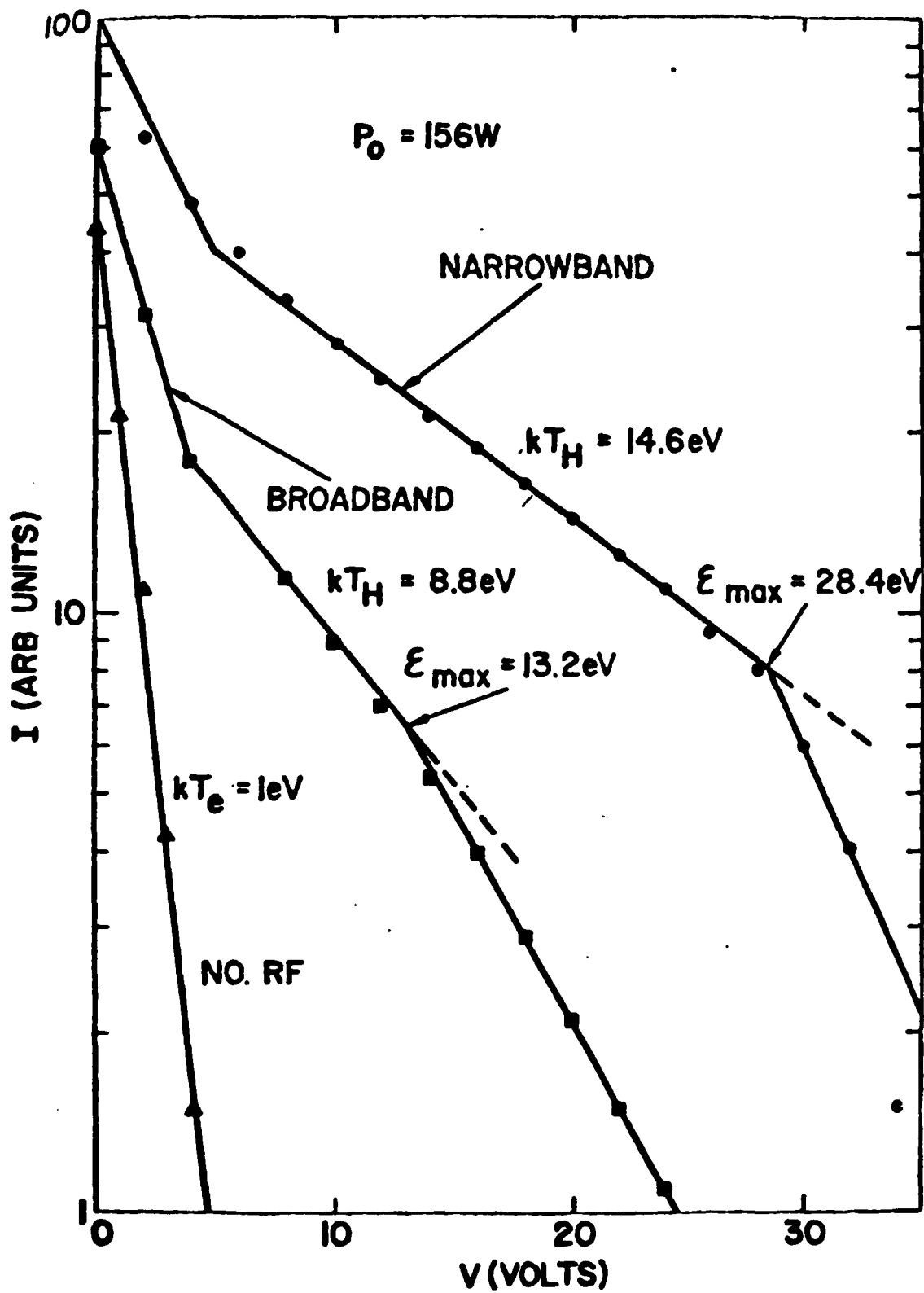
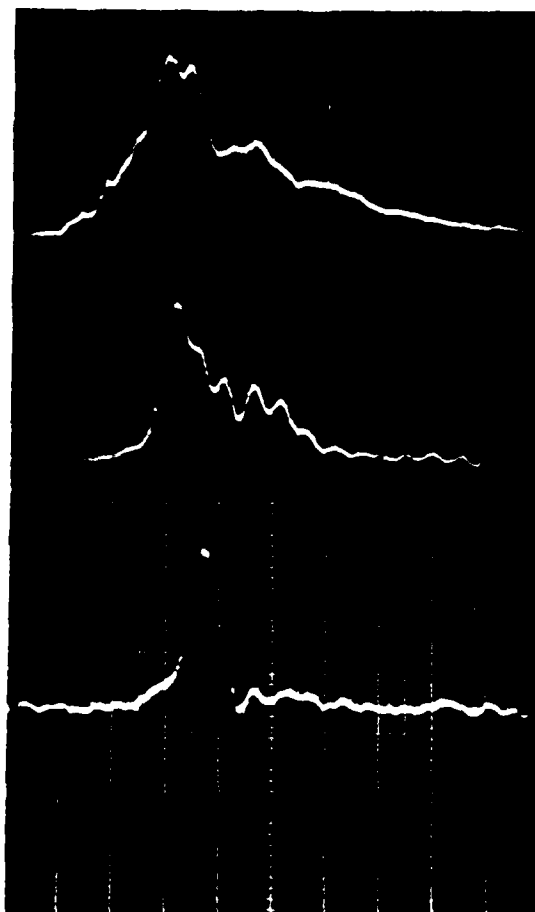


Fig. 22 Energy Analyzer Current as a Function of Analyzer Voltage for Cases of no rf, narrowband rf and Finite Bandwidth rf.

E_1^2
(FUNDAMENTAL)

E_2^2
(SECOND
HARMONIC)

E_3^2
(THIRD
HARMONIC)



200 ns/div

Fig. 23 Time Histories of Electric Field Intensities (Fundamental, second and third harmonic) in the Vicinity of the Critical Layer.

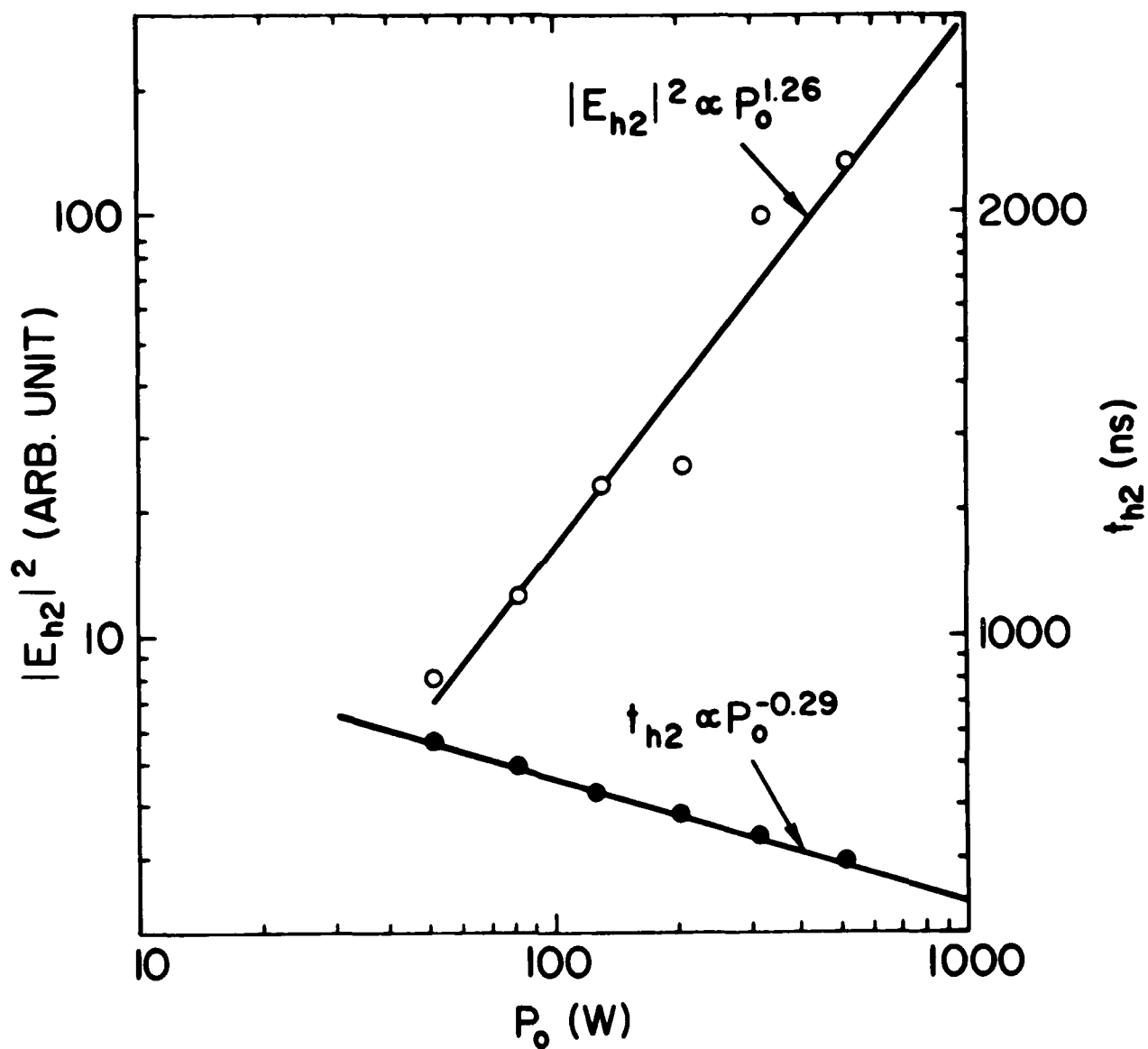


Fig. 24 Second Harmonic Electric Field Intensity and Breaking Time versus Incident rf Power.

initial normalized magnitude of the sinusoidal density perturbation. This predicts that at $P=500W$ and $\Delta=0.1$ the magnitude of the second and third harmonics are respectively 32dB and 56dB below the fundamental in good agreement with the measured values of 38dB and 58dB.

The spatial and temporal distribution of the electric field components were investigated in more detail. First, to investigate energy flow, the time at which the peak electric field occurred was determined as a function of axial position (up and down the density gradient). The results are shown in Figs. 25 and 26 for the fundamental and second harmonic, respectively. As can be seen, the energy appears to propagate both up and down the density gradient (from the cutoff layer) with a velocity of $0.1 v_{te}$ and $0.5 v_{te}$, respectively. The upstream energy vanishes at the critical layer at which point density streamers^(14,15) are ejected up and down the density gradient with the acoustic velocity. Details of the behavior on the ion time scale will be the subject of subsequent work. As expected, the spatial localization of the electric field is pronounced and increases for the higher harmonics.

As a final confirmation of the wavebreaking saturation interpretation, direct measurements of the plasma waves were made interferometrically by mixing a fixed reference probe signal with that from a movable probe. As can be seen from Figs. 27 and 28, the wave character is quite different at low and moderate powers. Specifically, at higher power levels we observe shorter wavelength components indicative of wave steepening and breaking. The probe places a lower bound ($\approx 1mm$) on the observable wavelengths. It should be noted that the slow variation (on the spatial scale) of the curves reflects the expected Airy function pattern.

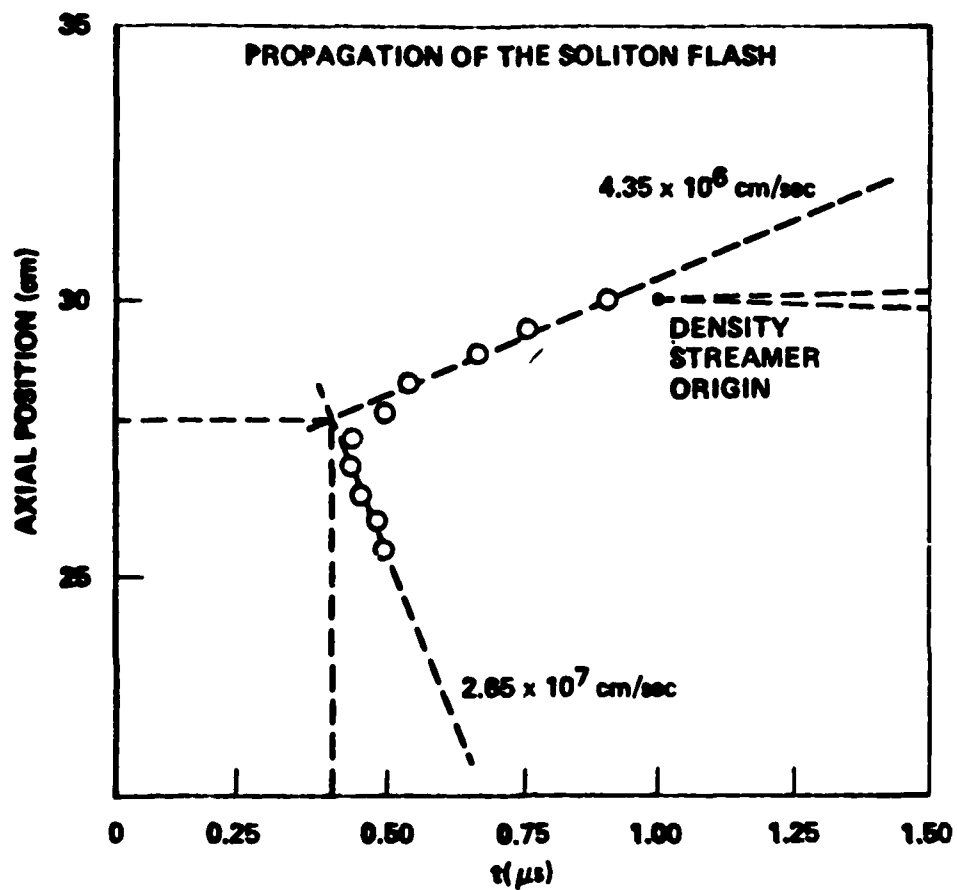


Fig. 25 Axial Propagation of Electric Field Intensity Maximum as a Function of Time After Turn-on of rf Pulse.

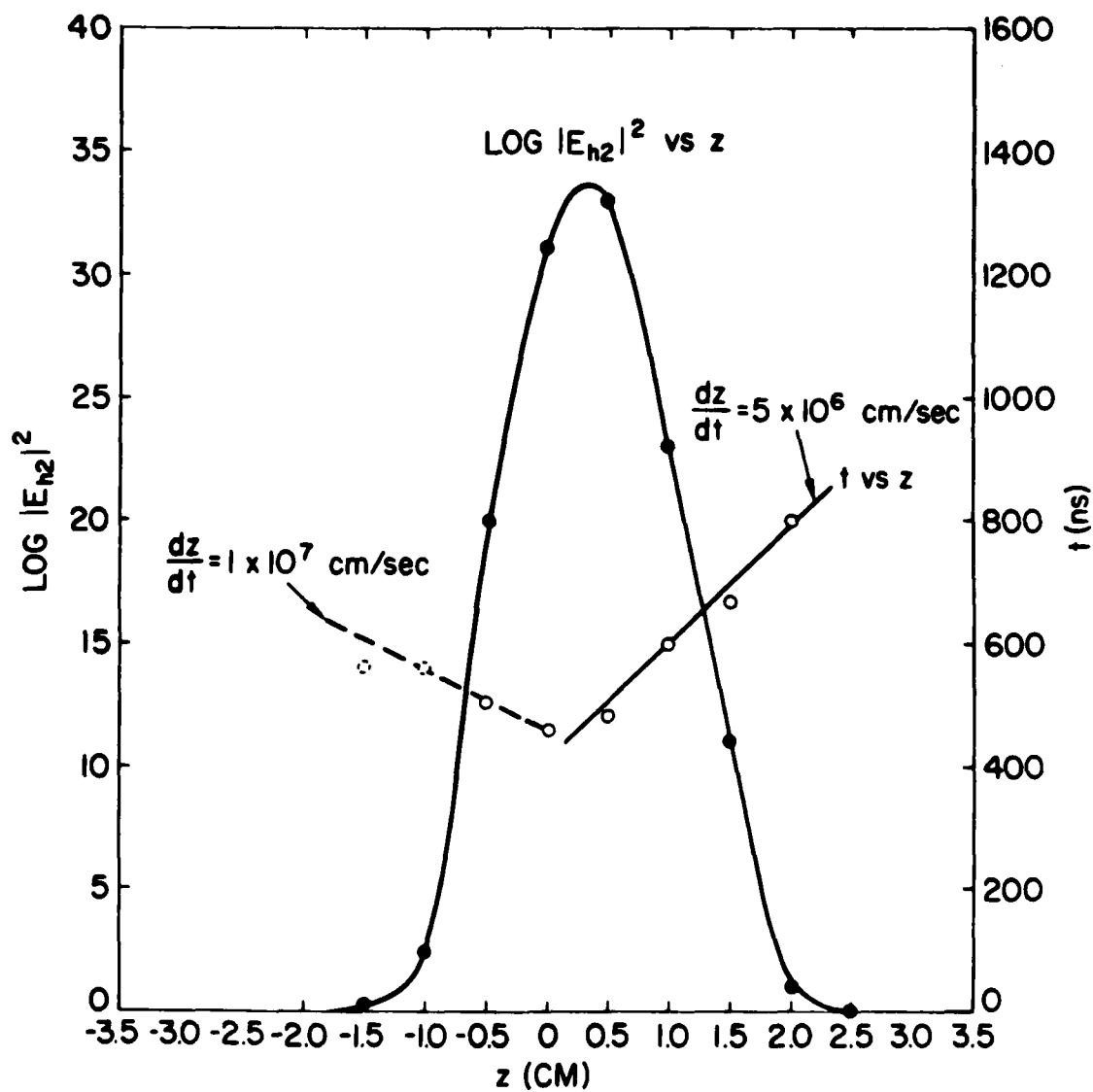


Fig. 26 Spatial Scan of the Second Harmonic.

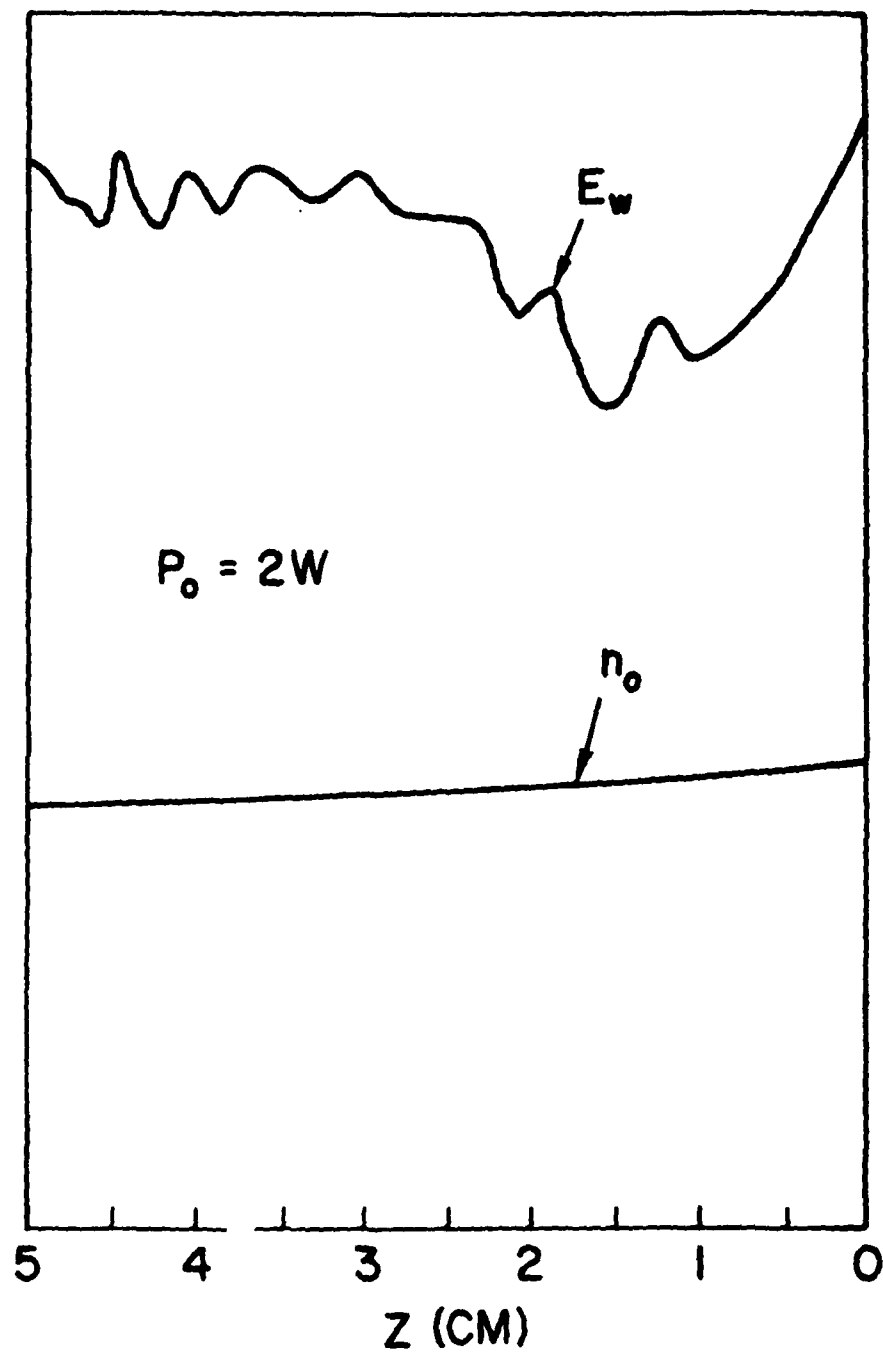


Fig. 27 Plasma Wave Propagation at Low Incident Power.

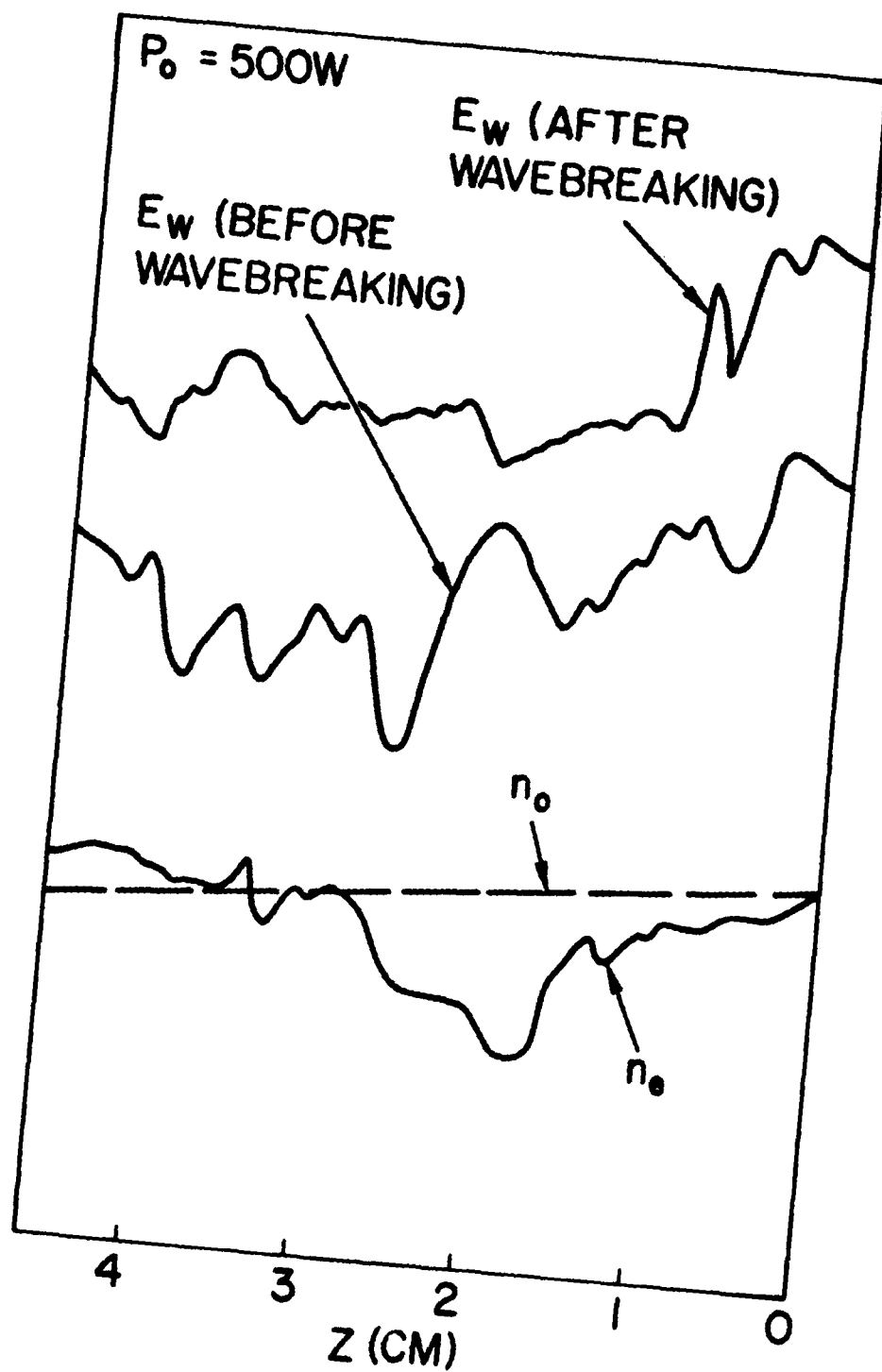


Fig. 28 Plasma Wave Distortion at Higher Incident Power.

As we saw earlier in Fig. 20, finite bandwidth slows down the growth of the resonance absorption produced electric fields and reduces the hot electron production. In this work, the bandwidth was produced by random amplitude modulation of the pump. However, it should be noted that studies were also performed with random phase modulation as well as with a coherent comb type pump (discrete lines). As long as the bandwidth was sufficiently large ($\Delta\omega t_p > 1$) or the number of lines large enough the results were similar.

The effects of finite bandwidth are shown quantitatively in Fig. 29. Here the measured wavebreaking time and critical layer electric field intensity are plotted in Fig. 27 as a function of the bandwidth of a random amplitude modulated pump (solid lines theory). The agreement is seen to be excellent.

Since the effects of finite bandwidth on the suprathermal electron distribution are of great interest, detailed measurements of the electron distribution were made as a function of bandwidth. A sample distribution was shown earlier in Fig. 23. As anticipated, finite bandwidth reduces both the hot electron tail temperature T_h and the upper cutoff energy E_m . Figure 30 shows the measured T_h and E_m versus pump bandwidth for an incident power of 150W. We see that the cutoff energy $E_m \propto (\Delta\omega/\omega_0)^{-0.67}$ in close agreement with the predicted $(\Delta\omega/\omega_0)^{-2/3}$ scaling. It is interesting that the hot electron temperature T_h scales very differently with bandwidth ($T_h \propto (\Delta\omega/\omega_0)^{-0.31}$). The changed hot electron temperature dependence may be due to the fact that in the finite bandwidth case, the resonant interval is increased and electrons may ride more than a single wave in traversing the field structure in breaking. Spielman et al.⁽¹⁶⁾ observed a similar bandwidth effect on T_h in a microwave experiment concerned with the time-asymptotic steady-state heated electron distribution. However, the most striking and important effect appears to be the reduction in

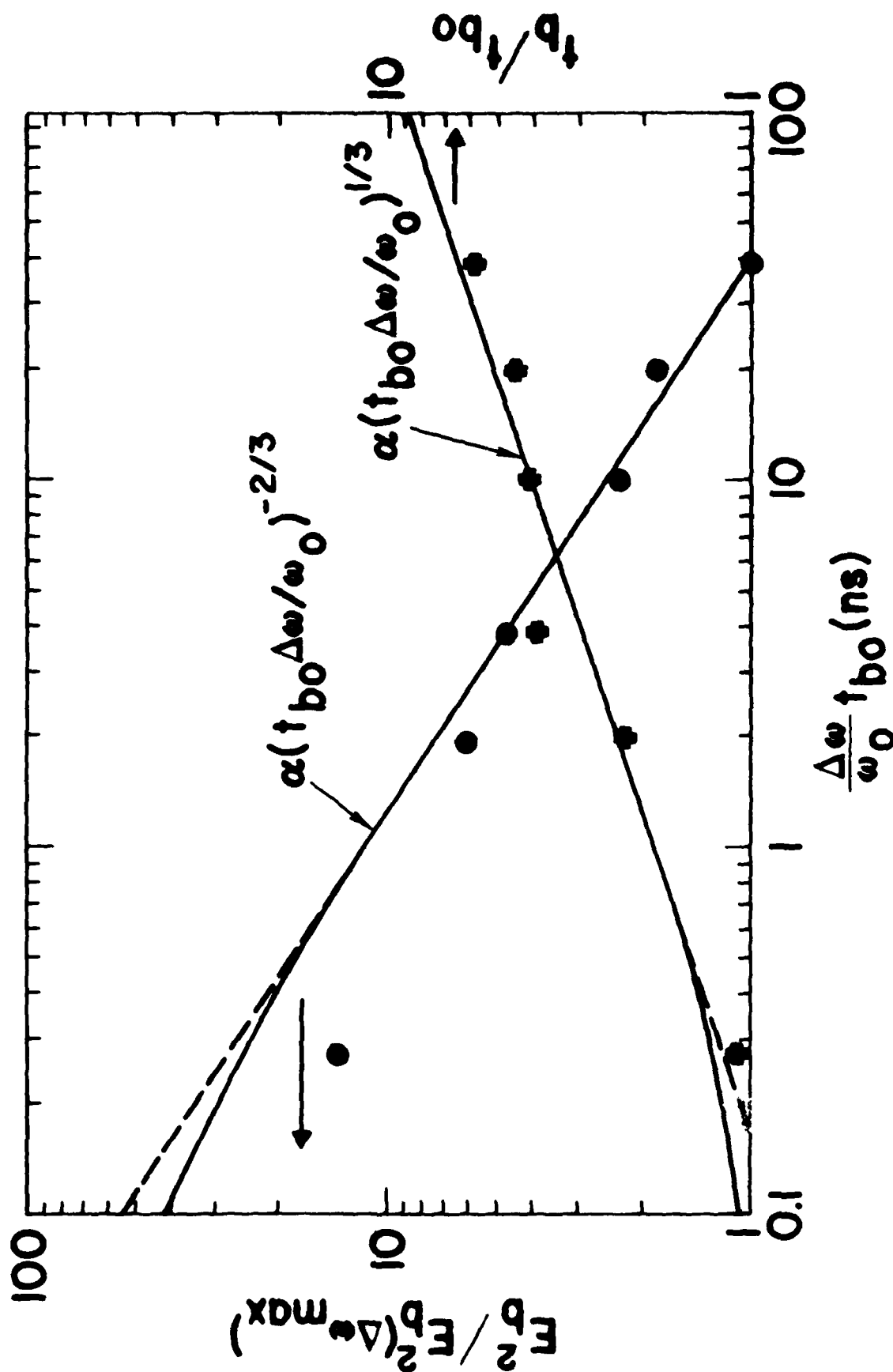


Fig. 29 Wavebreaking Field and Wavebreaking Time as a Function of Pump Bandwidth, $P_0 = 520 \text{ W}$, $f_0 = 2.8 \text{ GHz}$.

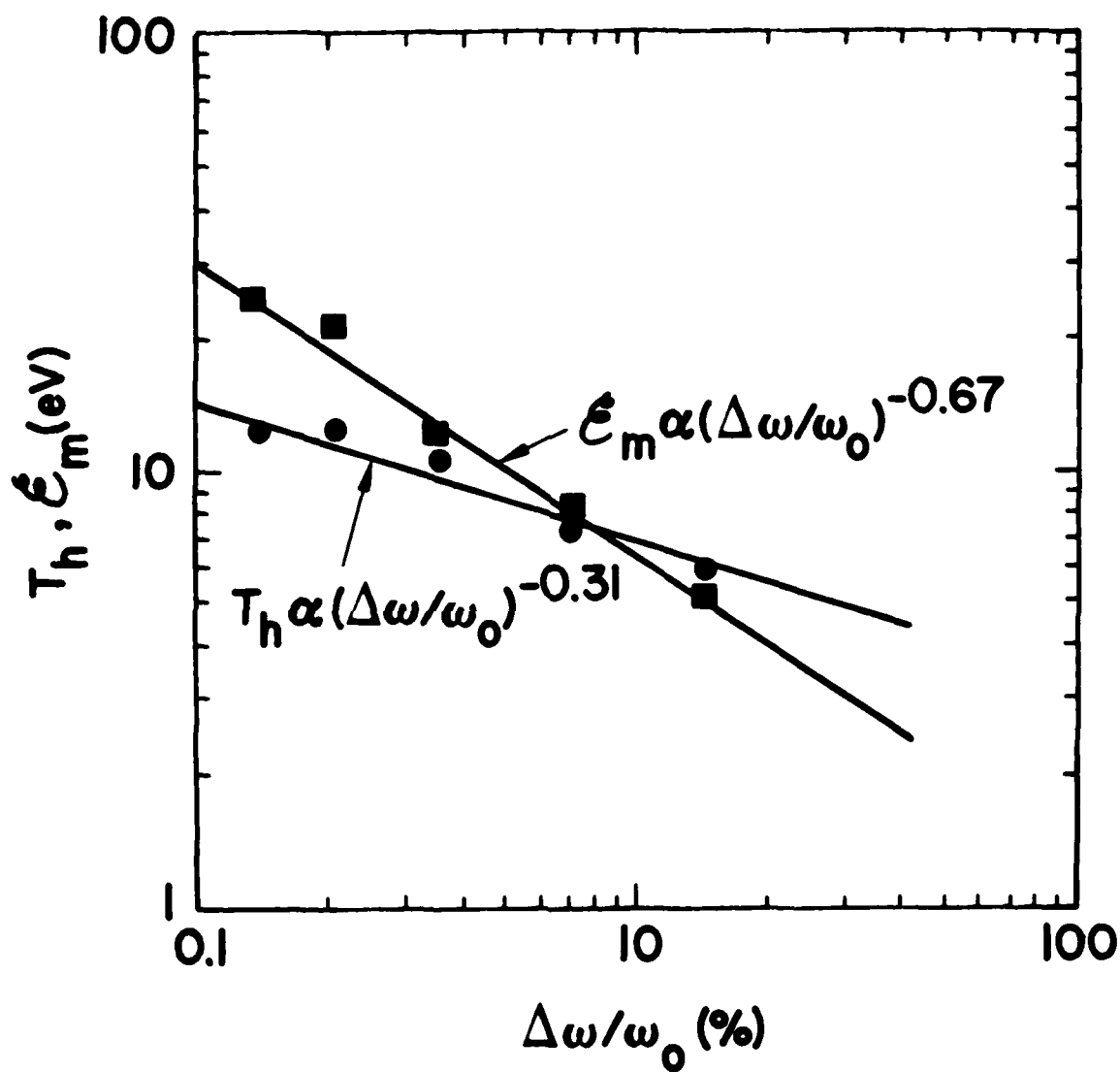


Fig. 30 Hot Electron Temperature and Maximum Energy as a Function of the Pump Bandwidth.

$\bar{\epsilon}_m$ observed in our experiment and predicted theoretically.

The effect of finite bandwidth on the hot electron density was also studied. As shown in Fig. 31, the total number of hot electrons decreases as the bandwidth is increased ($n_h \propto (\Delta\omega/\omega_0)^{-0.43}$). This is not explained by the fixed profile cold plasma model. There the amount of energy deposited through resonance absorption is predicted to be independent of bandwidth. This would imply that n_h should increase with bandwidth to compensate for the decrease in T_h and $\bar{\epsilon}_m$. A possible explanation for this discrepancy is that in the present experiment the density profile is not completely fixed but undergoes some modest profile modification which is bandwidth dependent. Specifically, we find that finite bandwidth results in considerable reductions in profile modification (2.7% versus 14% for the data shown) which could in turn change the total absorption. Presently, we are trying to see why some of our experimental results are in apparent disagreement with the predictions of Randall et al. (11)

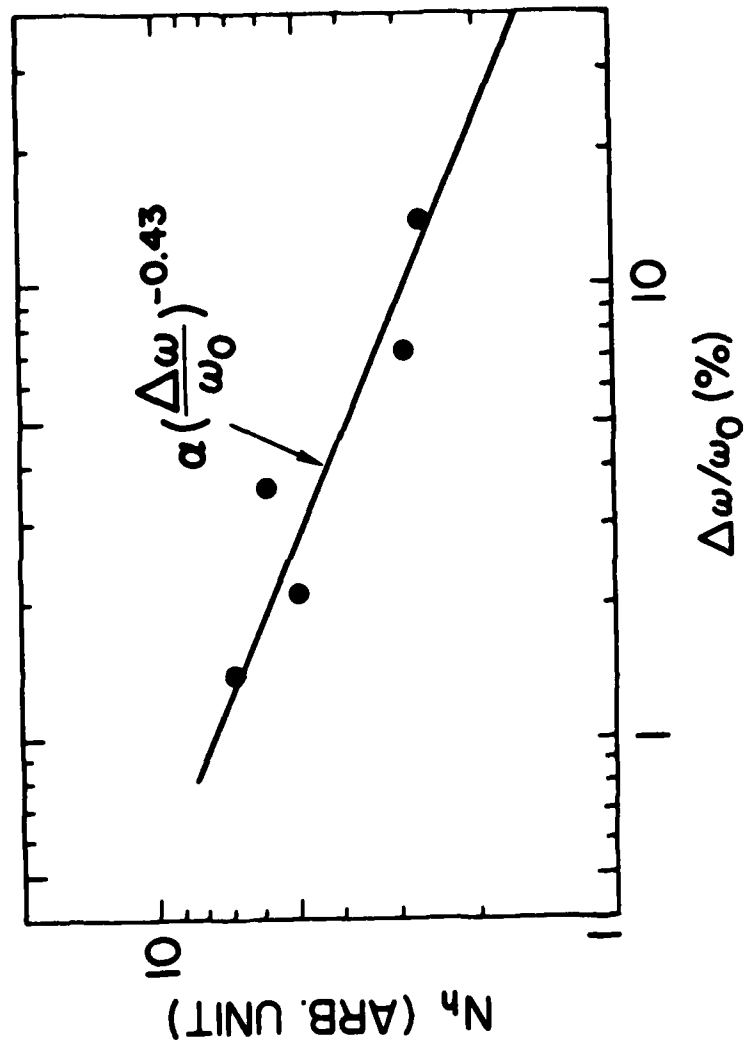


Fig. 31 Number of Accelerated Electrons as a Function of the Pump Bandwidth.

III. REFERENCES

1. Huey, H., A. Mase, N.C. Luhmann, R., W.K. DiVergilio, and J.J. Thomson, Phys. Rev. Lett. 45, 795 (1980).
2. Mase, A., N.C. Luhmann, Jr., J. Holt, H. Huey, M. Rhodes, W.F. DiVergilio, J.J. Thomson and C.J. Randall, Proc. of 8th IAEA Conf. on Plasma Physics and Controlled Nuclear Fusion Res., Brussels, Belgium, June 1980, Vol. II, pg. 745.
3. Thomson, J.J. and C.J. Randall, 11th Anomalous Absorption Conf., Montreal, Canada (1981).
4. Thomson, J.J. and W.F. DiVergilio, Final Report DOE Contract #DE-AC08-79DP40116 (1980).
5. Forslund, D.W., J. McKindel and B.L. Lindman, Phys. Fluids 18, 1002 (1975).
6. Kruer, W.L., Phys. Fluids 23, 1273 (1980).
7. Kruer, W.L. and K.G. Estabrook, UCRL Report #83743 (1979).
8. Kruer, W.L., E.J. Valeo and K.G. Estabrook. Phys. Rev. Lett. 35, 1076 (1975).
9. Williams, E.A. and J.R. Albritton, Paper C-2 9th Annual Conf. on Anomalous Absorption of Electromagnetic Waves, May 15-18 (1979).
10. Speziale, T., 9th Annual Conf. on Anomalous Absorption of Electromagnetic Waves, May 15-18 (1979).
11. Randall, C.J., J.R. Albritton and E.A. Williams, Bull. Am. Phys. Soc. 26, 971 (1981).
12. Randall, C.J., private communication (1981).
13. Davidson, R.C., Methods in Nonlinear Plasma Theory, Academic Press, Inc. (New York) pg. 38 (1972).
14. Elsasser, K. and H. Schamel, Plasma Phys. , 1055 (1977).
15. Morales, G.J. and Y.C. Lee, Phys. Fluids 20, 1135 (1977).
16. Spielman, R.B., W.M. Bollen, K. Mizuno and J.S. DeGroot, Phys. Rev. Lett. 46, 821 (1981).

